

NICMOS observations of high redshift radio galaxies: witnessing the formation of bright elliptical galaxies?

L. Pentericci^{1,3}, P.J. McCarthy², H.J.A. Röttgering³, G.K. Miley³, W.J.M. van Breugel⁴ and R. Fosbury⁵

ABSTRACT

We present the results of a near infrared imaging program of a sample of 19 radio galaxies with redshift between 1.7 and 3.2, using the NICMOS Camera 2 on the Hubble Space Telescope. The galaxies were observed in H-band which, for 18 of the 19 targets, samples the rest-frame optical emission longwards of the 4000 Å break. For many sources this band contains emission lines, but we estimated that this causes relatively little confusion in most cases.

The high angular resolution of the HST allows a detailed study of the host galaxies. The images show a wide range of morphologies, including (i) compact systems, (ii) systems with substructures such as multiple emission peaks and (iii) systems comprised of several components spread over areas of up to 100 kpc. Three galaxies appear unresolved and in two others a nuclear point source dominates the emission in the central region.

The morphologies of some of the lowest redshift targets are well represented by de Vaucouleurs profiles, consistent with them being elliptical galaxies. Their average effective radius derived is a factor of 2 smaller than that of $z \sim 1$ 3CR radio galaxies at similar restframe wavelength.

The near infrared continuum light is generally well aligned with the radio axis and the aligned light is very red, with typical V-H colors of ~ 3.5 –4. For several

¹Max Planck Institute für Astronomie, Königstuhl 17, D-69117 Heidelberg, Germany

²The Observatories of the Carnegie Institution of Washington, 813 Santa Barbara Street, Pasadena, CA 91101 USA

³Leiden Observatory, P.O. Box 9513, 2300 RA Leiden, The Netherlands

⁴Institute of Geophysics and Planetary Physics, Lawrence Livermore National Laboratory, PO Box 808, Livermore, CA 94459 USA

⁵Space Telescope European Coordinating Facility, Karl-Schwarzschild-Strasse 2, 85748 Garching, Germany

galaxies where WFPC2 V or R-band images were available we computed a high resolution map of the optical-to-infrared spectral indices: all multi-component systems present net color differences between the various clumps, and we argue that most probably the continuum emission has a stellar origin. Indicative ages of these stellar populations, as determined by the amplitude of the 4000 Å break vary between 0.5 and 1.3 Gyrs.

Finally in many of the small NICMOS frames we observe nearby faint objects close to the high redshift radio galaxies. The number density of these faint objects is slightly higher than that observed in the deep NICMOS parallel observations of random fields: furthermore these objects tend to be aligned with the direction of the main axis of the radio sources, suggesting that they may be related to the presence of the AGN.

1. Introduction

The study of the early Universe has received a considerable boost in the past few years, due to the development of new techniques for finding large numbers of galaxies at high redshift (e.g. U and B band dropouts, Steidel et al. 1996). Although radio galaxies are no longer the only class of well studied high redshift galaxies, they remain of exceptional cosmological interest, since they are likely to be amongst the most massive galaxies known in the early Universe and may be the progenitors of brightest cluster galaxies observed at low redshift. Their large masses can be inferred from their K-band luminosities and the near-IR K-z Hubble diagram (e.g. van Breugel et al. 1998). Furthermore there is evidence that they are undergoing vigorous star formation: at least in some high redshift radio galaxies (HzRGs) the UV continuum is dominated by young stars, with estimated star-formation (SF) rates of up to $1000 M_{\odot} \text{ yr}^{-1}$ (Dey et al. 1997). Sub-millimeter continuum dust emission has been detected in several of the highest redshift galaxies (e.g. Papadopoulos et al. 2000), also implying similar large SF rates. These stars are expected to settle on dynamical time-scales and evolve into fully developed elliptical galaxies.

Evidence that HzRGs might be located in proto-cluster environments includes: (i) the recent discovery of a megaparsec-scale structure of more than 15 Ly α emitting galaxies around the radio galaxy MRC 1138–262 at $z = 2.156$ (Pentericci et al. 2000a); around this same radio galaxy, the detection of luminous X-ray emission which is probably extended and has been attributed to a hot cluster atmosphere (Carilli et al. 1998); (ii) large Faraday rotation of the polarized radio emission indicating that some HzRGs are surrounded by dense hot magnetized cluster gas (Carilli et al. 1997; Pentericci et al. 2000b); (iii) excess of companion galaxies detected along the axes or in the vicinity of the radio sources (Röttgering et al. 1996); (iv)

possible excess of Lyman break selected galaxies in the fields of several other powerful radio sources (e.g. Lacy & Rawlings 1996) and in particular several candidate companion galaxies (with two objects spectroscopically confirmed) in the vicinity of MRC 0316–257, at $z=3.14$ (Le Fevre et al. 1996; McCarthy et al. 1992), and a number of faint red companions of 4C 41.17 at $z=3.8$ detected from deep Keck imaging at $2\ \mu\text{m}$ (Graham et al. 1994). Having both large stellar masses (e.g. 4C41.17 with $M\sim 10^{11}M_{\odot}$, van Breugel et al. 1998) and high star formation rates (see above), and being located in the densest regions of the early Universe, it is natural to propose that HzRGs will evolve into present-day brightest clusters galaxies (e.g. Best et al. 1998).

In previous papers we have described our studies of HzRGs with the Hubble Space Telescope at optical (UV rest-frame) wavelengths (Pentericci et al. 1998 and 1999). It was found that several HzRGs, such as MRC 1138–262 at $z=2.2$ and 4C41.17 at $z=3.8$ (Dey et al. 1997) are comprised of numerous continuum clumps embedded in giant (~ 100 kpc) diffuse Ly α halos. Such morphologies are strikingly similar to simulations of forming bright cluster galaxies, made on the basis of the hierarchical models, which predict that the most massive systems are assembled from smaller building blocks (e.g. Baron and White 1987; Dubinski 1998). Indeed the sizes, profiles and luminosities of the *individual* clumps are similar to those of the Lyman break galaxies (LBG) (e.g. Steidel et al. 1996, Giavalisco et al. 1996), indicating that HzRGs could be formed by an assembly of LBGs (Pentericci et al. 1998).

The well known alignment observed between the rest-frame UV morphology and the radio axis (Chambers et al. 1987, McCarthy et al. 1987) implies that the UV emission is strongly effected by the active galactic nucleus, e.g. by scattered light from a QSO or a young population of stars whose formation is triggered by the passage of the radio jet. Studies of the near-infrared morphology (rest-frame optical) are particularly important to reveal the nature of the older stellar population (e.g. Lilly 1988), although observations of the continuum emission are made difficult by the presence of strong emission lines in the near-IR bands (Eales & Rawlings 1993).

There have been extensive ground-based near-IR studies of powerful radio galaxies at intermediate and high redshift (e.g. Eisenhardt and Chokshi 1990; McCarthy et al. 1992; Eales et al. 1997; Best et al. 1998; van Breugel et al. 1998). The most important results of these searches are: (i) the morphologies of $z\sim 1$ galaxies in the near-IR emission are considerably more relaxed and symmetric than in the optical emission; surface photometry of 3CR $z\sim 1$ galaxies has shown that they follow a de Vaucouleurs law (Best et al. 1998), implying that they are dynamically evolved systems (e.g. Rigler and Lilly 1994) with inferred stellar masses of up to $10^{12}M_{\odot}$; (ii) 3CR radio galaxies show a possible excess of emission at large radii, resembling the halo that surrounds nearby cD galaxies (Best et al. 1998); (iii) models of spectral energy distributions of radio galaxies having redshifts between 1 and 3 have

been used to infer the ages of their stellar populations, suggesting ages in excess of 1 Gyr and formation redshift of $z \sim 5$ or higher (e.g. McCarthy 1993b, Lilly 1988); (iv) deep near infrared (K-band) imaging reveal clustering of red galaxies around some $z \sim 1$ 3CR galaxies (e.g. Roche et al. 1998; Best 2000); (v) van Breugel et al. (1998) found strong evolution of the morphology of HzRGs at rest frame visual ($> 4000 \text{ \AA}$) wavelengths, from aligned galaxies at redshift > 3 to more symmetrical and compact galaxies at $z < 3$.

With NICMOS it is possible to study the near infrared morphology of HzRGs to a resolution comparable to that of our optical WFPC2 images, allowing us to investigate the morphologies of their evolved stellar populations at redshift larger than 2. We can then address questions such as whether there are already well formed ellipticals at those epochs; the importance and the frequencies of merging with sub-galactic clumps at different epochs; how the presence of substructures evolves with redshift; the relationship between the radio source and the near infrared emission in the central regions of the galaxies. In particular, one can examine to what extent the optical/UV alignment effect is also present at near infrared wavelengths.

In this paper we present NICMOS observations of a sample of 19 radio galaxies with $1.8 \leq z \leq 3.2$. In Section 2 we describe the sample selection and the observations. Section 3 is devoted to the presentation of the results, and a description of the morphologies of the individual objects. In Section 4 we analyze the morphologies of the galaxies and their optical-to-infrared colors; we then discuss the implication of our NICMOS results for the study of the alignment effect and we investigate the statistics of (aligned) companion galaxies around the targets.

2. Observations

2.1. Sample selection

Two sub-samples of objects were observed. The first sub-sample consists of 14 radio galaxies from the Molonglo Reference Catalog (MRC) (McCarthy et al. 1996). The MRC/1Jy sample was defined simply using a flux density limit at 408 MHz of $S_{408} \geq 0.95 \text{ Jy}$, within a restricted region of the sky ($-30 < \text{DEC} < -20$, $|b| > 15$); 99.5% of the sources in the catalog have been optically identified, and 46 of the 426 radio galaxies in the sample have spectroscopically confirmed redshift $1.6 < z < 3.2$ (see McCarthy et al. 1990 and McCarthy et al. 1991 for the optical identification and spectroscopy of the higher redshift galaxies). The MRC/1Jy survey is one of the largest complete radio sample for which there is a homogeneous and nearly complete set of optical and infrared photometry (see the mentioned papers and McCarthy et al. 1992 for infrared observations).

We then added 5 targets selected from a sample of ultra steep spectrum radio galaxies (USS).

This sample comprises the largest set of radio galaxies having redshift larger than 2, which were selected on the basis of the radio spectral indices ($\alpha \leq -1.1$ where $S_\nu = S_0\nu^\alpha$). This selection technique has proven to be the most effective tool for identifying such radio galaxies. Several samples of USS sources (e.g. Chambers et al. 1996, Röttgering et al. 1994) have led to the discovery of more than 80 radio galaxies with $z > 2$, about 60% of the 150 such sources known to date (e.g. van Breugel et al. 1999). All the highest redshift radio galaxies ($z > 3.5$) have been found using this technique (e.g. van Breugel et al. 1999). The USS sample covers a larger area in the sky than the MRC sample, and allows us to probe a wider range of radio sources parameters such as their luminosity and size. Furthermore selecting sources from the USS sample will give a larger overlap with the existing data base of WFPC2 images (Pentericci et al. 1999).

The final sample consists of 19 radio galaxies, uniformly spanning a redshift range between $z = 1.68$ and $z = 3.13$, and having a large range of properties, e.g. a range of nearly 3 magnitudes in the infrared luminosity and a factor of 8 in radio power. The radio galaxies are listed in Table 1: for each object we report the redshift, the position of the radio core, the total flux at 4.7 GHz, the spectral index between 4.7 and 8.2 GHz, $\alpha_{8.2}^{4.7}$, the total size in arcseconds and an indication of the radio morphology.

2.2. Observations and data reduction

2.2.1. *HST/NICMOS*

In Table 2 we list the radio galaxies observed and various observational parameters. All objects were observed with NICMOS Camera 2, which has a plate scale of 0.0762×0.0755 arcseconds per pixel and a total field of view of $19.2'' \times 19.2''$. The filter used was the F160W filter, which is centered at $1.6 \mu\text{m}$, has a bandwidth of $0.4 \mu\text{m}$ and has the minimum background amongst the available NICMOS filters; we also used the F165M filter which is centered at $1.7 \mu\text{m}$ and has a bandwidth of $0.2 \mu\text{m}$. We had initially selected this second filter for many of the objects, because it would have provided a bandpass free from line emission for most of the galaxies in the sample, in particular those in the lowest and in the highest redshift ranges ($z < 2.09$ and $z > 2.6$). Unfortunately using this filter the response was limited by readout-noise and dark current and we had to change our initial observing strategy to use the F160W filter. The wider filter bandwidth included bright emission lines for many of the sources (see Table 2), but we estimate that in most cases this causes relatively little confusion in determining their real continuum morphologies (however see next section). The high sensitivity of this filter allowed the galaxies to be mapped within the allocated 2 to 5 orbits per object.

Each orbit included two 1026 seconds exposures using the MIF1024 Multiaccum exposure sequence and one shorter exposure using the STEP64 sampling sequence. The exposure times for the STEP64 samples were 384, 411, 512 or 576 seconds depending on the orbit. The total integration time for each galaxy is given in Table 2. To facilitate removal of residual flat field and imperfection of the detector, the targets were offset by $\sim 3''$ between each exposure, giving a grid of 15, 12, 9 or 6 exposures.

The NICMOS imaging data were processed in the following manner: the zero level determined from the first read of each exposure sequence was subtracted from all other exposures; then a scaled version of the best dark exposure provided by the HST archive was subtracted. The resulting sequences of “read” in each Multiaccum or STEP64 series were then used to produce a masked, linearized and, to first order, cosmic ray rejected image using an algorithm written by McLeod (1997). Then for the exposures which were obtained before August 1997 the pedestal level (i.e. significant fluctuations of the zero level between sequences) was subtracted separately from each quadrant of the HgCdTe detector and again the cosmic ray rejection algorithm was used. For the observations taken after August 1997 the last two steps could be skipped. Finally, the images were flat fielded using the best flat field provided from the HST archive. The images were then registered using fractional pixel shifts, and were combined using a mask for removal of bad pixels and hot pixels (this mask was constructed directly using the observation frames) and a multi pass $\pm 3\sigma$ cosmic ray rejection algorithm. In combining the images, we weighted them using their exposure times.

2.2.2. Supporting ground-based observations

For 3 radio galaxies in the sample (MRC 0156–252, MRC 0406–244 and MRC 2104–242) we gathered extensive ground-based optical and near-IR data during the last few years. In Table 3 we summarize the relevant observations. Some results on MRC 0406–244 were already published by Rush et al. 1997.

For the spectroscopic observations at the ESO/NTT Telescope, the detector was a Tektronix CCD with 1024^2 pixels and a scale along the slit of $0.37''$ per pixels. The CCD was binned by a factor of two in the wavelength direction. Using a $2.5''$ wide slit with ESO grating #3 we achieved a spectral resolution of 2.8 \AA (full width at half maximum, FWHM). The raw spectra were bias subtracted and flat fielded; the sky contribution was then removed by subtracting a sky-spectrum obtained avoiding the regions where the target was positioned; finally wavelength calibration was performed by measuring the position on the CCD of known lines from a He-Ar calibration lamp, fitting a polynomial function to these data and applying the resultant calibration factors. The accuracy of the calibration is better than 0.3 \AA .

The J and K images were obtained with the Las Campanas du Pont 2.5m telescope and

its 256×256 HgCdTe array camera, which has a pixel scale of $0.35''$. The integration times ranged from 4000 to 9000 seconds and the objects were moved on the array every 150 seconds. The data were calibrated with standard stars from Elias et al. (1983). The reduction followed standard techniques. The r , I and $\text{Ly}\alpha$ images were also obtained at Las Campanas using a 800×800 Texas Instruments CCD detector: the exposures were binned 2×2 resulting in a pixel scale of $0.332''$. The $\text{Ly}\alpha$ images were obtained with interference filters having 1% band-widths. Several 1800 second exposures of each field were obtained, with approximately $10''$ offsets between each image.

All data were reduced using standard IRAF procedures. The various images were then registered with the NICMOS frames using the position of several point sources in the field, with the AIPS (Astronomical Image Processing System) tasks XTRAN and HGEOM, assuming a linear transformation. The accuracy of the registration is about $0.2''$.

All the radio galaxies with the exceptions listed below were imaged with the VLA in A-array as part of a high resolution, multi-frequency radio polarimetric study carried out on a large sample of HzRGs; for further details about the observations see Carilli et al. (1997). For a subset of galaxies, new VLA observations were carried out: the radio galaxies MRC 0324–228 and MRC 0350–279 were observed in the B-array configuration at 4.85 GHz (C-band). The radio galaxies MRC 0152–209, MRC 1017–220, MRC 2048–272 and MRC 2224–273 were observed in the A-array configuration as part of a new high resolution multi-frequency radio survey. Details of these observations have been presented elsewhere (Pentericci et al. 2000b).

2.3. Emission-line contamination

As explained earlier we observed most of our targets with the F160W broad band filter. This resulted in the unavoidable inclusion of bright emission lines normally found in radio galaxies. For the lowest redshift object (MRC 2224–273 at $z = 1.68$), the strong emission line $\text{H}\alpha$ falls in the observed wavelength range; for the objects in the redshift range $1.9 < z < 2.6$, [OIII] and $\text{H}\beta$ become important; finally for the higher redshift objects ($z \geq 2.9$) the emission line [OII] is within the observed wavelength range. In Table 2 we have listed, for each object, the lines that can contribute substantially to the continuum band flux and the total estimated contribution to the continuum flux.

Since we do not have direct measurements for the line fluxes and their equivalent widths, we have estimated the total contaminating flux using other measured lines (in most cases $\text{Ly}\alpha$ and/or $\text{H}\alpha$). We have used the emission line ratio reported by McCarthy (1993) and Eales & Rawlings (1996), i.e. $\text{Ly}\alpha/[\text{OII}] = 5$, $[\text{OIII}]/[\text{OII}] = 3$, $\text{Ly}\alpha/\text{H}\alpha = 1.6$. Note however that these are only average ratios. For example, Eales & Rawlings (1993) find that the line

emission ratios can vary significantly (within a factor of 10) from object to object, due to the different physical conditions of the gas and/or the presence of dust which can attenuate the Ly α line (e.g. in USS 0211–122, van Ojik et al. 1994). Another important source of uncertainty is the difference in the apertures used to derive the continuum and line fluxes: the continuum flux was measured through a fixed 4'' diameter aperture, while the line fluxes (mostly taken from the literature) were measured within different apertures and with slits of different sizes. When the apertures used to determine the emission line flux were known (in about half of the cases) we corrected for this by simply scaling the line flux to an aperture of 4''. Therefore the values for the emission line contamination given in Table 2 are only indicative. Most important, the line contribution may vary spatially and some parts of the galaxies might be more affected than others, with a much higher line contribution than that listed in Table 2.

2.4. Astrometry

The coordinate frame for the NICMOS images determined from the image header information has uncertainties of the order of 0.6'' due to the uncertainty in the position of the guide star (HST data handbook). Since the optical galaxies are generally clumpy on a scale of a few tenths of arcsecond, it is important to obtain the better relative registration between the radio and the optical images for a detailed inter-comparison.

Our radio maps have a typical resolution of 0.2'' which is comparable to that of the NICMOS images. The exceptions are the radio maps of MRC 0324–228 and MRC 0350–279 which have a resolution of 1.2''.

To align the NICMOS and the radio VLA images we overlaid the radio cores (for the identification of radio cores see Carilli et al. 1997 and Pentericci et al. 2000) on the peak position of the near infrared emission, on the assumption that this IR peak coincides with the galaxy nucleus. In these cases the estimated uncertainty in the overlay is $\sim 0.1''$. In the cases of MRC 0324–218, MRC 0943–242, USS 1707+105 and MRC 2048–272 where no radio core was detected, we used the absolute HST and VLA astrometry to align the maps; in these cases the accuracy achieved is only $\sim 0.8''$.

3. Results

3.1. Summary

In Figures 1 to 19 we present the images of the radio galaxies. In most cases we show grey scale representations of the NICMOS emission with VLA contours superimposed (unless the radio emission is unresolved) and a contour map of the continuum emission to better delineate the morphology of the central regions (for all sources except the three unresolved ones).

In Table 4 we list the total NICMOS H-band magnitudes for each object, derived using a fixed 4'' circular aperture. The errors in the magnitudes, reported in column 5, are dominated by the inaccuracy in the sky subtraction. For those galaxies that have more components, we also report the magnitudes of the other clumps brighter than 23.5: the letters in Table 4 refer to the components as labeled in the figures. For MRC 1138–262 and USS 1707+105 we kept the same nomenclature as previous papers (Pentericci et al. 1998;1999).

The NICMOS H-band 3σ limiting surface brightnesses achieved ranges from $\mu_{H(3\sigma)} = 24.8$ to $\mu_{H(3\sigma)} = 25.1$ (see Table 2) for the objects that were imaged with the F160W filter and only $\mu_{H(3\sigma)} = 23.7$ for those observed with the F165M filters and for shorter exposure times. In almost all cases the signal to noise ratio is good and allows us to study in detail the morphology of the galaxies. The exceptions are the very faint radio galaxy MRC 0324–228 at $z = 1.89$ and the highest redshift object in the sample, MRC 0316–257 at $z = 3.13$.

Our observations show that HzRGs have a wide variety of near-infrared morphologies. Of the 19 galaxies, 3 are unresolved (MRC 0350–279, MRC 1017–220, USS 2202+128); of these, the first 2 are also unresolved in the radio at all frequencies and MRC 1017–220 has been classified as a broad line radio galaxy (BLRG) by Kapahi et al. (1998) on the basis of its emission line spectrum. In two other cases, MRC 1138–262 and MRC 2025–218, a nuclear point source dominates the emission in the central regions, but there is clearly underlying extended emission. For all other systems no nuclear point source contributes substantially to the emission. The morphologies of the galaxies vary from compact or unresolved structures to systems comprised of several components spread over large areas (up to 100 kpc). A large fraction of the systems shows close (within $\sim 5''$) emission clumps, that might be part of the systems, but only in few cases, where additional information is available (e.g. narrow band imaging, spectroscopy, etc.) we can conclude that these small components are physically associated to the radio galaxies.

Comparison with the radio sources shows that typically the near infrared emission is well aligned with the radio axis. The alignment effect will be extensively discussed in Section 4. In the next subsection we will make some remarks on the individual objects.

3.2. Individual objects

MRC 0140-257 $z = 2.64$

The galaxy is shown in Fig. 1: it has 2 peaks of emission with almost the same flux. The orientation of the line joining these peaks is, within a few degrees, along the radio axis. It is possible that the observed morphology is due to an obscuring dust lane. There are a few fainter clumps within 2-3'' of the galaxy that could be physically associated with the system.

MRC 0152-209 $z = 1.89$

The galaxy is shown in Fig. 2: it is elongated and it is surrounded by a halo of fainter emission. There is a narrow elongated tail that departs from the southern end of the galaxy. The radio source is unresolved.

MRC 0156-252 $z = 2.09$

This galaxy is shown in Figs. 3 and 20a-d and is discussed more extensively in Section 3.3.

USS 0211-122 $z = 2.34$

The host galaxy (Fig. 4) of this very large (134 kpc) radio source consists of a nucleus plus faint diffuse emission, having the shape of an arc. The galaxy is misaligned with respect to the radio axis; however the radio source shows a jet feature extending from the core towards south, whose curvature suggests that the radio axis might be precessing.

MRC 0316-257 $z = 3.13$

The galaxy is shown in Fig. 5. There are two objects separated by only $\sim 2''$. The identification is the fainter diffuse object to the west. The other object could well be at the same redshift. Given the high redshift of this radio galaxy, the NICMOS image samples rest-frame continuum emission that is mostly below the 4000 Å break, therefore we are not really imaging the older stellar population.

MRC 0324-228 $z = 1.89$

The galaxy is shown in Fig. 6. There are two faint and diffuse objects separated by only $\sim 1.5''$ which could be identified as the host galaxy of the radio source. Ground-based observations do not resolve the 2 components (McCarthy et al. 1996), which could be part of the same system; alternatively, one could be the radio galaxy and the other just a foreground object. The VLA snapshot radio image at 4.5 GHz with a resolution of 1.2'', shows a simple double radio source with no core detected. The direction of the radio axis is at 25° with respect to the relative orientation of the two emission clumps.

MRC 0350-279 $z = 1.90$

The identification of this radio source is the unresolved object in Fig. 7. There are two faint objects at a distance of only $6''$ to the east: one of them is compact and the other one diffuse and elongated. The radio source is unresolved in our VLA B-array snapshot observation, so we do not show it.

MRC 0406-244 $z = 2.44$

This galaxy is shown in Figs. 8 and 21a-d and is discussed further in Section 3.3.

MRC 0943-242 $z = 2.93$

This galaxy is shown in Fig. 9: it has a cigar shape and is elongated along the radio axis. The WFPC2 optical image is remarkably similar. The galaxy is extensively discussed in McCarthy et al. 2000 (in preparation).

MRC 1017-220 $z = 1.77$

The identification of this radio source is the unresolved object in Fig. 10. There are 2 faint diffuse clumps about $5''$ away. The radio source is also unresolved. Kaphai et al. (1998) have classified this radio galaxy as a BLRG on the basis of its emission line spectrum.

MRC 1138-262 $z = 2.16$

The central object of this very large system in Fig. 11 has a large contribution from a nuclear point source, but clearly there is extended emission below it. In addition several other components are visible in a region of about $10'' \times 10''$ around the nucleus: all have WFPC2 optical counterparts, and are embedded in a giant $\text{Ly}\alpha$ halo. This galaxy is further discussed in Pentericci et al. 1997 and 1998.

USS 1410-001 $z = 2.33$

This is a very elongated object (Fig. 12), consisting of the galaxy core plus 2 other clear peaks and diffuse emission extending for more than $4''$ along the galaxy axis. The very red ($V-H=5.6$) and compact object only $2''$ from the core, might also be part of the system. The galaxy and the radio source are strongly misaligned: the angle between the optical and radio axis is nearly 45° . However, the northern component of the radio source is curved, suggesting the radio axis might be precessing, in which case the elongated near infrared emission could be extended along the previous position of the radio jet.

USS 1707+105 $z = 2.35$

This is a large multiple system (Fig. 13) consisting of 2 or possibly 3 different galaxies (see Pentericci et al. 1999) separated by $3-4''$ and located along the radio axis. The radio core is

not detected in the present radio image, however it seems most likely that the radio emission comes from the most luminous and larger galaxy, centrally located between the two radio lobes that is indicated with the letter A in Fig. 13. This galaxy is comprised of a main body plus a few smaller clumps and shows diffuse emission towards north, along the direction of the radio axis, but also perpendicular to it.

MRC 2025-218 $z = 2.63$

The galaxy is shown in Fig. 14. The emission is dominated by a nuclear point source. Once this is subtracted there is a large diffuse galaxy roughly aligned with the radio axis. The radio source is small and the southern radio jet presents a sharp bent.

MRC 2048-272 $z = 2.06$

The galaxy is shown in Fig. 15. Two bright objects can be seen separated only by $2.5''$ with a third faint object $2''$ to the east. With the present astrometry the correct identification is probably the central object. The radio core is undetected in our VLA radio images.

MRC 2104-242 $z = 2.49$

This galaxy is shown in Figs. 16 and 23a-c, and is discussed more extensively in Section 3.3.

USS 2202+128 $z = 2.70$

The object (Fig. 17) is not resolved on the present image. The radio source is small and s-shaped suggesting the radio axis might be precessing.

MRC 2224-273 $z = 1.68$

This galaxy (Fig. 18) has a simple pear-shaped morphology. There is a small compact object only $2.6''$ away, located along in the direction of the galaxy main axis. The radio source is unresolved at all frequencies in our VLA observations (Pentericci et al. 2000b).

USS 2349+280 $z = 2.89$

The galaxy is shown in Fig. 19: it consists of 2 components embedded in a halo of diffuse emission. The sharpness of the separation between the two components suggest that it could be due to a dust lane (the NICMOS image samples the emission interval 3600-4630 Å, which can be still effected strongly by dust). The WFPC optical image is very similar (Chambers et al. 1996).

3.3. Detailed multi-wavelength comparisons

MRC 0156-252

In Fig. 20a-c we show the NICMOS image in grey scale overlaid with contours from (a) the I-band emission, (b) the K-band emission and (c) the Ly α narrow band emission. In Fig. 20d we show in grey scale the radio jets at 8.2 GHz superimposed on Ly α narrow band contours. The I-band contains nearly pure continuum emission, with the relatively weak MgII 2798 line falling at one end of the filter band; the K-band is contaminated by the H α emission line falling at the lower edge of the filter; finally the NICMOS H-band contains a contribution from the [OIII] line (see Table 2).

The emission from the ionized gas is very extended ($\sim 9''$) and is not associated with the optical and near infrared emission; the Ly α does not follow the optical/near infrared components, but peaks at the location where the radio jet bends sharply. This case is very similar to that of MRC 1138–262 (Pentericci et al. 1997) and 1243+036 (van Ojik et al. 1996): the most likely interpretation is that a cloud of ionized gas is responsible for the deflection of the radio jet, and that the gas emission is strongly enhanced in this region due to shock ionization. Note also that the optical galaxy is located at a minimum of the Ly α emission, a common feature of many HzRGs (e.g. MRC 1138–262 and MRC 2104–242 below).

Another interesting feature of MRC 0156–252 is the presence of two smaller components aligned (within 5°) with the the radio axis but located *beyond* the radio hot-spots. They are of comparable brightness in the H-band (see Table 4), but the easternmost clump, labeled C in Fig. 3, is much redder than clump B. This difference in colors may be due to a difference in age of the stellar population: McCarthy et al. 1992 argued on the basis of ground-based data that the central galaxy contains a very old stellar populations (~ 2.8 Gyrs) or alternatively a very reddened QSO spectrum. The bluer colors of component B, which is located near the bent in the radio jet, might be interpreted as enhanced star formation induced by the passage of the jet (e.g. Best et al. 1997)

MRC 0406-244

This galaxy is extensively discussed in Rush et al. (1997). In Fig. 21a-c we show the NICMOS image in grey scale overlaid with contours from (a) the I-band emission, (b) the K-band emission and (c) the Ly α narrow band emission. In Fig. 21d we show in grey scale the radio jets at 8.2 GHz superimposed to Ly α narrow band contours. The K and H filters contain contributions from line emission: in particular the K-band contain the strong H α + [N II] $\lambda\lambda 6548, 6584$ system and the H-band contains the [OIII] $\lambda\lambda 4959, 5007$ lines. The I-band is purely continuum emission.

The main body of the galaxy shows two emission peaks, and a number of components distributed in a sort of envelope on both sides. The galaxy along the radio axis, which coincides

remarkably well with a radio peak, is most probably at a different redshift (Rush et al. 1997). There is a spatial shift in the peak of the emission at different wavelengths: the peak of the I-band coincides with that of H-band while the K-band peak probably lies in between the two NICMOS peaks, although due to the lower resolution ($0.9''$) and larger pixels size of this image, with the present overlay we cannot exclude that the K-band peaks coincides with the brightest H-band peak.

The net color gradient between the northern side and the southern was interpreted by Rush et al. (1997) with the fact that most of the emission in the southeast extension is the result of line contamination. The northwest components that appear in the I-band are probably true continuum flux.

A high resolution spectrum of the Ly α line taken along the direction of the radio axis is presented in Fig. 22. The spectrum has a total spatial extent of $\sim 8''$, similar to the extent seen in the narrow band image. The emission comes from two components which are offset both in space ($\sim 2''$) and velocity (~ 1150 km sec $^{-1}$); with the help of the narrow band image we identify the brightest component with the main body of the galaxy, while the other component is the northwestern extension. They have both a FWHM of ~ 850 km sec $^{-1}$. An interesting feature is the deep trough which maybe due to absorption by associated neutral hydrogen, a feature common to many HzRGs (van Ojik et al. 1997). The neutral gas is as spatially extended as the ionized gas and has a velocity gradient of ~ 200 km sec $^{-1}$.

MRC 2104-242

In Fig. 23a-c we show the NICMOS image in grey scale overlaid with contours from (a) the R-band emission, (b) the K-band emission and (c) the Ly α narrow band emission. Note the residuals of a spike of a bright nearby star located to the north of the radio galaxy. We do not show an overlay of the Ly α gas with the radio emission since the radio hot-spots are located further beyond the region of the gas emission (see the radio map in Fig. 16). The radio axis is oriented at 12° (counterclockwise), implying that both the continuum and line emission are well aligned with it. In Fig. 24 we present a high resolution spectrum of the Ly α line.

The galaxy is comprised of several components, each having very different colors: (i) the nucleus of the radio galaxy, which has a very red color $V - H \sim 5$, (ii) a series of smaller bluer clumps northern of it; (iii) a narrow elongated feature to the south.

As in MRC 0156–262, the nucleus coincides with a minimum of Ly α emission. To the north of it, a bright component is clearly seen in R-band and is associated with the brightest Ly α emission, which at this position has a FWHM of ~ 500 km sec $^{-1}$, a rather low value compared with average HzRGs, but consistent with the relation found by van Ojik (1995) that the largest radio sources tend to have Ly α emission with lower velocity dispersion.

Finally, the narrow elongated feature is associated with spectacular Ly α emission, which

has 3 different peaks, having velocities of 140 km sec^{-1} , 670 km sec^{-1} and 990 km sec^{-1} blue-wards of the central Ly α emission. The overall velocity dispersion of the system is 1270 km sec^{-1} (FWHM).

Note that the Ly α spectrum shows that the Ly α emission extends beyond that seen in the Ly α image and spans a total region of $\sim 14''$, as large as the radio source.

4. Discussion

4.1. Morphologies: when do the first elliptical galaxies appear?

One of the most interesting problems in cosmology is at what epoch elliptical galaxies formed. To study this issue, we tried to determine if any of the host galaxies of these distant radio sources has a morphology that resembles that of elliptical galaxies, and if so, determine their characteristic parameters and their dependence with redshift.

When possible, we fitted the radially averaged surface brightness profiles of the host galaxies with the most commonly used model distributions: de Vaucouleurs and exponential. This was not done for (i) the 3 unresolved galaxies and (ii) the 2 galaxies in which the emission in the central region is dominated by a point source. In these last cases, although we could subtract a central point source revealing the extended underlying galaxies, the subtraction was not good enough to allow a fit of the residual.

Whenever there were companions in the vicinity of the main galaxy to be fit, they were subtracted and replaced by an average background value.

For 9 out of 14 galaxies, the fit gave meaningless results, in particular for those having more than one peak of emission within the main body of the galaxy (e.g. MRC 0406–244) and for those with an irregular morphology. Also some apparently regular galaxies (such as MRC 0943–242) are not well represented by any of the above laws. For 5 of the galaxies (namely MRC 0152–209, USS 0211–122, USS 1707+105A, MRC 2048–272 and MRC 2224–273), the surface brightness profile could be well represented by a de Vaucouleurs law, while the exponential profile gave worst results. In Fig. 25 we show the fit that we have obtained for these radio galaxies, and in Table 5 we report the best fit parameters, r_e and μ_e , that were determined by minimizing the χ^2 . We also report the values of the reduced chi-squared, which indicates that the fit are quite good in all cases.

The average effective radius for the 5 galaxies is $r_e = 5.4 \pm 1.6 \text{ kpc}$ (adopting $H_0 = 50 \text{ km sec}^{-1} \text{ Mpc}^{-1}$, and $q_0=0.5$), with a median value of 5.3 kpc .

The PSF of NICMOS might influence the result of the fit. It is difficult to recover accurately its shape since the NIC 2 frames are very small and contain none or few point sources; furthermore it is known that the PSF of NICMOS varies both spatially and with time (Colina

and Rieke 1997). Only for USS 1707+105 we could construct a model of the PSF using 2 non-saturated point sources near the radio galaxy. We then de-convolved the frame of USS 1707+105 and fitted again the image obtained: the resulting parameters r_e and μ_e are, within the error, comparable to those obtained by fitting the original image. So we are confident that, at least for the 3 largest galaxies (namely USS 0211–122, USS 1707+105A and MRC 0152–209), the PSF does not influence the results of the fit.

Another possible source of confusion might be the presence of spatially extended line emission, especially if this is distributed differently from the continuum emission. However as we see from Table 2, line emission should be negligible in all cases except for MRC 2224–273, where it contributes for $\sim 30\%$ of the total H-band flux.

We emphasize that while the good fit to the $R^{1/4}$ law suggests that these galaxies might be morphologically ellipticals/bulges, a knowledge of the spectral energy distribution is also needed to fully determine their nature.

It is interesting to notice that all the galaxies which can be well represented by the de Vaucouleurs law, are in the lowest part of our redshift range (below $z \sim 2.4$). This hints to a possible redshift evolution, although there is not net dependence of morphology on redshift. We can compare these results to what is obtained for lower redshift 3CR radio galaxies. It is well known that a large fraction ($\sim 80\%$) of the $z \sim 1$ radio galaxies have profiles which are well fit by a de Vaucouleurs law (e.g. Best et al. 1998; McLure et al. 2000). In particular McLure et al. (2000) derived basic parameters for a sample of $z \sim 1$ 3CR radio galaxies from I-band WFPC2 images (using F814W or F785LP filters). These images have a resolution similar to ours; in addition we selected from their sample, a sub-group of objects such that the rest-frame emission sampled by the observations was as similar as possible to that of our 5 galaxies. In practice we selected the 9 galaxies where the rest-frame range sampled was fully above the 4000 Å break. These galaxies are at a median redshift of 0.75. Their average r_e is 11.9 ± 2.4 kpc, with a median value of 8.5 kpc.

Although the two samples are small, the indication is that the $z \sim 2$ radio galaxies are at least a factor of 2 smaller than the lower redshift radio galaxies. Only one high redshift galaxy (USS 1707+105A) has a radius comparable to its lower redshift counterparts. For reference, brightest cluster ellipticals in the local universe have an average effective radius of 32 kpc, and values vary from 10 kpc to several tens of kpc (e.g. Schombert 1988).

The above results indicate that a dynamically relaxed and relatively old stellar population is already in place in most of the $z \sim 1$ systems, while it becomes rarer at redshift $z \sim 2$ and disappears at even higher redshift. A possible evolutionary scenario for the hosts of powerful radio galaxies that can be inferred from these results is the following: at redshifts from 3.5 to ~ 2.5 most galaxies show considerable substructure and clumpiness, suggesting strong interactions and mergers. At $z \sim 2$ some host galaxies appear morphologically re-

laxed; between $z \sim 2$ and $z \sim 1$ almost all systems (up to 80 %) evolve into fully developed elliptical galaxies and during this time the characteristic scale length of the galaxies increases on average by a factor of 2. As argued by Best et al. (1998) these galaxies will then continue to accumulate matter through mergers and gas infall: if the mergers occurs homologously (e.g. Schombert 1987), a merger of a large galaxy with a small systems gives as a result a remnant with a larger radius and a more diffuse morphology as compared to the original galaxy. In this way the hosts of high redshift radio galaxies would then evolve into present day brightest cluster galaxies.

4.2. Colors: comparison between WFPC2 and NICMOS morphologies

For those objects (8) that have both the WFPC2 and NICMOS images, we constructed a color index map in the following way. The optical images were initially convolved with a Gaussian function to bring them to the same resolution as the near infrared ones ($0.2''$). For the galaxies USS 0211–122, MRC 0943–242, MRC 1138–242, USS 1410–001, USS 1707+105, MRC 2025–218 and MRC 2104–242 that were imaged with the planetary camera (Pentericci et al. 1998,1999) we re-binned both frames on a finer pixel scale; using factors of 3 and 5 for the WFPC2 and the NICMOS respectively, the final pixel scales agreed to better than 1.3%. For the galaxy MRC 0406–242 which has been imaged on the WF3 chip (Rush et al. 1997), the factors used were 4 and 3 respectively for the WFPC2 and the NICMOS, and the agreement between the final scales was better than 2%.

The WFPC2 and NICMOS images were aligned by comparing the location of stars that were present on both frames. If this was not possible (e.g. because on the small NICMOS frame there were no point sources) we used the location of distinct peaks of the radio galaxy itself. We only applied integer shifts to avoid interpolation. After sky subtraction we calibrated both images to units of flux density in μJy , using the information in the headers of the WFPC2 images and the calibration of the NICMOS Camera 2 filters derived by Colina and Rieke (1997).

Finally we derived color maps as:

$$\text{COLOR} = \log(S_{WFPC2}) - \log(S_{NICMOS}),$$

excluding all pixels having fluxes less than 3σ (where σ is the rms noise), and re-binned the final image by averaging regions of 2×2 pixels. The resulting image can be calibrated on a scale of two-point spectral index α , where $S_\nu \sim \nu^{-\alpha}$, or alternatively can be scaled to magnitude color index as: (i) $R-H=1.17+0.91\alpha$, for those galaxies that were imaged with the F702W filter (all galaxies at redshift beyond 2.9), or (ii) $V-H=1.40+1.08\alpha$ for those that were imaged with the F606W filter (all other galaxies).

The resulting maps of two-point spectral index are presented in Figs. 26-29. Note that there

are some spurious color structures, like sharp pixel to pixel variations, especially at the edges of some small components, due to regions with very different signal to noise in the 2 colors, the difference in PSF shape, and the uncertainty of $\sim 0.1''$ in the alignment procedure.

We shall use these color maps in the next section to study the alignment effect. Here we just examine the distribution of the color indices and their possible relations to other properties of the radio sources.

We limit this study to the clumpiest objects, which have a complex color index distribution, i.e. the four galaxies MRC 0406–244, MRC 1138–262, USS 1707+105 and MRC 2104–242. We measured the color index in different regions of the above galaxies by averaging over a circle with $\sim 0.2''$ radius around the peaks in the emission present in the WFPC2 image and/or in the NICMOS image (some components are present only in one of the two bands). We only considered regions of emission that are surely part of the systems i.e. that emit Ly α at the same redshift and/or are embedded in the Ly α halo of the galaxies. In Fig. 30 we present an histogram with the distribution of optical to infrared spectral indices. The median color index is around $\alpha = 2$ and more than 75% of the components have spectral indices between 1.5 and 3 (corresponding to V-H colors between 3 and 4.6), indicating that the radio galaxies contain very red regions.

Note that since the redder bands is in some cases (e.g. MRC 2104–242, see Table 2) contaminated by line emission, a very irregular and clumpy distribution of the emitting gas could produce sharp color gradients between the various components.

Since many properties of HzRGs depend on radio size (e.g. van Ojik et al. 1997) it is interesting to determine if there is a correlation between the color index of the clumps and their distance from the radio core. The results are show in Fig. 31: there’s no evident relation between the distance of the component and its color. We also looked at a possible correlation between the color index of a component and the relative position angle of the component with respect to the radio axis: again we see no correlation. Therefore we conclude that the colors of the aligned components of HzRGs, don’t vary much with radio size and orientation, although presenting a large scatter. Note however that the statistics is small and that there is not a large variation in size between the 4 galaxies considered, so this could mask possible relations.

4.3. The radio/near-infrared alignment effect

Our images show that the near-infrared continuum emission of HzRGs is generally aligned with the main axis of the radio emission. This is the so-called alignment effect which has been studied for more than a decade. Several models have been proposed to explain its nature (for a review see McCarthy 1993a and references therein), the most viable

ones being: (i) star-formation stimulated by the radio jet as it propagates outward from the nucleus (Chambers et al. 1987; McCarthy et al. 1987; de Young 1989; Daly 1990); (ii) scattering of light from an obscured nucleus by dust or free electrons (di Serego Alighieri et al. 1989; Scarrot et al. 1990; Tadhunter et al. 1992; Cimatti et al. 1993); (iii) nebular continuum emission from warm line emitting clouds (Dickson et al. 1995). There is evidence that all these mechanisms contribute to the alignment effect, with strong variations from object to object (e.g. Pentericci et al. 1999). We will try to assess their contribution using the new near-infrared images and the color maps constructed in the previous section.

Assuming that a considerable fraction of the blue light is scattered light from a central quasar (see for example Cimatti et al. 1994), we can estimate the percentage of scattered light there would be in the H-band. According to unification models the incident spectrum seen by the scattering medium is that of a quasar, $S \propto \nu^{-\beta}$ (we use β to distinguish this parameter from the optical-to-infrared spectral index, defined as α). As a value for β we take the one derived from the composite spectra of quasars from the MRC catalogue (the same parent catalogue from which most of our sources were taken) compiled by Baker and Hunstead (1995). They found $\beta = 1$ for the steeper cases. Thompson scattering by thermal electrons is wavelength independent (although in some cases it has serious energetic difficulties, e.g. Eales and Rawlings 1990): in this case the scattered spectrum will be in shape similar to the incident one. For dust scattering, the output spectrum will be bluer than the incident one (for optically thin dust), with the exact shape depending on the size of the grains (e.g. Dey et al. 1996 and references therein).

Assuming 50% of the blue flux (at $\sim 1800 \text{ \AA}$ rest-frame) is scattered light, and that the scattered component has a power-law spectrum with $\beta = 1$, we can calculate its contribution at $\sim 5000 \text{ \AA}$ for components with different observed optical-to-infrared spectral indices. The fraction of scattered light in the optical will also be 50% for those components with an observed spectral index $\alpha = 1$; it will be 26% for the components with an observed optical-to-infrared spectral index $\alpha = 2$; it will be 10% for those with an index $\alpha = 3$; and finally it will be 4% for the components with $\alpha = 4$. These percentages would decrease considerably if the scattering is wavelength dependent; on the other hand they could increase if we allow for some reddening. However it is clear that for components with observed optical-to-infrared spectra steeper than $\alpha \sim 2$, as most radio galaxies exhibit (see Fig. 30), scattered light cannot be the dominant fraction of the emission at 5000 \AA rest-frame wavelength.

We note that in some objects the aligned component has a nearly uniform spectral index whereas in other ones, whereas in other ones. To the first category belong the galaxies USS 0211–122, MRC 0943–242 USS 1410+001 and MRC 2025–218 (although this last case is more complicated due to the presence of a strong unresolved nuclear component), where the aligned light has a nearly constant spectral index (~ 2.3 for USS 0211–122 and MRC

2025–218, and ~ 2 for MRC 0943–242 and USS 1410+001).

For two of these objects there exist also polarization measurements, showing that the rest-frame UV emission is polarized: USS 1410–001 has a polarization of 10% (Cimatti et al. 1998) and an estimated total contribution of scattered light of 40 to 60% (depending on the nature of the scatterer) at 1800 Å (rest-frame). MRC 2025–218 has a polarization of 8% (Cimatti et al. 1994), and the total SED of the galaxy can be fit by models in which scattered light accounts for a very large fraction of the emission at 1800 Å.

Then from the uniformity of the spectral indices in the aligned component, and using the calculations above, we conclude that in these objects also a considerable fraction (~ 30 –40% or more) of the rest-frame optical emission could be scattered light.

For the other galaxies (namely MRC 0406–244, MRC 1138–262, USS 1707+105 and MRC 2104–242) the optical-to-infrared color index varies considerably within the different regions. Furthermore, the spectral indices of some components are considerably steeper than $\alpha = 2$, and in some galaxies the components are located outside the ionization cone. In the source MRC 1138–262 if we were to draw such a cone so that all the continuum emission would line inside, it should have an half opening angle of at least 70° . This is much wider than what expected by models of AGN unification (up to 45° , e.g. Barthel 1989), and than values found through imaging of the the emission line regions in active galaxies: for example Wilson and Tsvetanov (1994) find average half opening angles of $\sim 30^\circ$. The same thing is valid for USS 1707+105A, which is clearly extended in a direction perpendicular to the radio source and therefore outside the ionization cone. These characteristics argue against scattering as a major contributor to the light, since in this case we would expect components with uniform and bluer colors (assuming that the properties of the scattering medium do not vary considerably amongst the various components). Hence we conclude that in these systems the contribution of scattered light to the optical continuum must be very small (less than 10%).

If we then assume that in these galaxies most of the emission is produced stellar light, we can derive an approximate age for the stellar population and compare it with the age of the radio sources, to determine whether jet-induced star formation could be a viable mechanism to account for the stellar population. To derive an *indicative* age for the stars, we have matched the amplitude of the 4000 Å break observed in the clumps with the amplitudes (at the same rest-frame wavelengths) derived from the spectral energy distributions of stellar populations evolving according to the galaxy isochrone synthesis spectral evolution library compiled by Bruzual and Charlot (1993). We used their 1995 model, assuming a simple stellar population, and a Salpeter initial mass function (IMF), with star masses ranging from 0.1 to $125 M_\odot$. The instantaneous star-burst model, which evolves most rapidly, can reproduce the observed 4000 Å break in 0.5 Gyrs for the bluest components of HzRGs, to 1.3 Gyr for the

reddest ones. All other modes of star formation (e.g. star-burst with a finite duration, an exponentially declining star formation mode, etc.) require a longer time to reproduce the same colors.

Clearly there are a number of uncertainties in this age determination, e.g. the inferred ages could be wrongly estimated in those components that have a contribution of line emission in any of the two bands. In any case the indication is that these components have rather large ages, of the order of half a Gyr or more.

The typical life-time of a radio source can be easily derived as $t=D/2v$, where v is the expansion speed of the hot-spots and D is the total extent of a radio source. The velocity v is typically in the range 0.01-0.2c (e.g. Alexander and Leahy 1987), and our sources have maximum extent of about 200 kpc. Therefore their lifetime will be in the range $0.2-3 \times 10^7$ yrs, i.e. about 100 times shorter than that of the stellar population. Note that alternative estimates of the radio source life-time, e.g. from spectral ageing arguments also in general lead to ages of $\sim 10^7$ yrs (Carilli et al. 1991). Clearly if the radio activity was recurrent then the observed clumps could have formed during previous phases of activity.

Finally we mention the model proposed by West (1994), in which the anisotropy of the optical and infrared emission around a typical high redshift radio galaxy is due to the anisotropy of the surrounding density distribution (see also Eales 1992). In this model, galaxy formation proceeds along preferred directions which are related to large scale elongated distribution of matter: in the prolate potential of the forming galaxy, the gas will fall and settle into a disk whose axis is along the major axis of the distribution of matter. The radio jets then will be emitted along this axis, hence the alignment between their direction and the distribution of the surrounding material (gas and stars). Within this model the relative ages of the radio jets and stellar components do not have to be matched. However, this model alone cannot explain the alignment effect since, for example, it cannot explain the polarization properties of many HzRGs.

4.4. Companion galaxies and their relation to the alignment effect

Most HzRGs in our sample show very close companion objects. We define a companion as a small (size $\leq 1''$) object that is located within a region delineated by a 100 kpc diameter around the radio source. We exclude objects with a stellar profile (although they might be in some cases high redshift unresolved objects, rather than stars) and those which can be recognized as spirals, on the assumption that they are most probably foreground systems. We do not consider the inner 30 kpc from the galaxy centers, to ensure that the regions of the source itself are excluded from the statistics (this is true in almost all cases except for the larger systems, but the overall result does not depend on them).

The average number of companion galaxies for the 19 HzRGs is 1.9 ± 0.3 down to a magnitude limit of $m_H = 23.5$. From deep counts of NICMOS parallel orbit, Yan et al. (1998) derive an average cumulative density of galaxies in H-band down to a magnitude $m_H = 23.5$ of $\sim 1.5 \times 10^5$ galaxies deg^{-2} . The expected number of galaxies in a circular area of radius 50 kpc is 1.4. Therefore there is a marginal (2σ) excess of objects in the area around HzRGs. We do not have any other systematic information on these possible companion galaxies, that might tell us about their real redshifts. However further evidence that these objects may be associated to the radio galaxies is provided by the distribution of the orientation of companions with respect to the radio axis (or optical axis if the radio source is unresolved). In computing this distribution we have excluded companions of the 2 radio galaxies that are unresolved both in the radio and in the near-infrared emission (MRC 0324–228 and MRC 1017–220) since in these cases it is impossible to determine any preferred direction. The result is presented in Fig. 32: the histogram shows that the companion galaxies are predominantly located along the radio axis. A Kolmogorov-Smirnov test shows that the distribution differs from a uniform distribution between 0° and 90° with 99% probability.

Röttgering et al. (1996) reported a similar effect, finding a statistical excess of optical companions located along the radio axis of USS radio sources. While they defined companions as objects that are located within a circle with diameter equal to the radio source extension, we prefer to use a fixed scale, since we do not assume a-priori that the companion galaxies are related to the presence of the radio sources. However it is significant that, even with a different definition, both groups find an excess density in the direction of the radio axis.

This result shows that the alignment effect not only holds for the radio galaxy hosts, but also for its neighboring galaxies within an area of at least ~ 100 kpc. An interesting issue would be also to determine how the overdensity and the alignment of these companion galaxies depend on the area considered. Unfortunately the NICMOS data are not useful in this respect, since the NIC 2 field of view is far too small.

The above conclusions show that any model attempting to explain the alignment effect has to take into account not only the morphology of the radio galaxies hosts, but also their surroundings (for the possible origin of the alignment effect see the discussion and the references in the previous section).

5. Conclusion

We have presented the results of a near infrared imaging program on a sample of 19 radio galaxies having redshift between 1.7 and 3.2, observed with NICMOS Camera 2 on the Hubble Space Telescope.

Our observations show that the host galaxies of powerful radio sources have a wide range of

morphologies, from systems with simple compact morphologies to systems with substructures such as multiple emission peaks to systems comprised of several components spread over large areas. Only in few cases the active nucleus dominates the emission in the central region.

Following is a summary of the most important results obtained:

(i) While most systems appear irregular, 5 galaxies at $z \sim 2$ have morphologies consistent with them being elliptical galaxies (or bulges), i.e. they can be well represented by the classical $R^{1/4}$ law. A comparison between this small sample and the host galaxies of $z \sim 1$ 3CR radio sources, observed at similar rest-frame wavelengths and resolution, indicates that there is difference of a factor 2 in their effective radii.

(ii) We find that in almost all extended systems the near infrared continuum light is aligned with the radio axis and the aligned component has very red colors. For several galaxies WFPC2 V or R-band images were available so we computed a high resolution map of the optical-to-infrared spectral index. These spectral indices are in general rather steep, $\alpha \sim 2$ or steeper. The clumpy systems show net color differences between the various components, which can be explained with different ages for the stellar content. Indicative ages determined from the Bruzual and Charlot models are of the order of ~ 0.5 -1 Gyr in most cases, much larger than typical radio source ages.

(iii) In the small NICMOS frames we can see in many cases nearby faint objects around the high redshift radio galaxies, and their space density is slightly higher than what is observed in the deep NICMOS parallel observations of random fields. Furthermore these objects tend to be aligned with the direction of the main axis of the radio sources suggesting that they are related to the presence of the radio galaxies.

This work is based on observations with the NASA/ESA Hubble Space Telescope, obtained at the Space Telescope Science Institute, which is operated by AURA Inc. under contract with NASA. HJAR acknowledges support from an EU twinning project, a programme subsidy granted by the Netherlands Organization for Scientific Research (NWO) and a NATO research grant. The work by WvB at IGPP/LLNL was performed under the auspices of the US Department of Energy under contract W-7405-ENG-48.

REFERENCES

- Alexander, P., Leahy, J.P. 1987, MNRAS, 225, 1
Baker, J.C., Hunstead, R.W. 1995, ApJ, 452, L95
Baron, E., White, S. D. M. 1987, ApJ, 322, 585

- Barthel, P. D. 1989, ApJ, 336, 606
- Best, P. 2000, MNRAS, in press
- Best, P., Longair, M. S., Röttgering H.J.A. 1998, MNRAS, 295, 549
- Best, P., Longair, M. S., Röttgering H.J.A. 1998, MNRAS, 286, 785
- Bruzual, A.G., Charlot, S. 1993 ApJ, 405, 538
- Carilli, C. L., Perley, R. A., Dreher, J. W. and Leahy, J. P. 1991, ApJ, 383, 554
- Carilli, C. L., Röttgering, H., van Ojik R., Miley, G. K., van Breugel, W. 1997, ApJS, 109, 1
- Carilli, C. L., Harris D., Pentericci, L., et al. 1998, ApJ, 494, 143
- Chambers, K. C., Miley, G. K., van Breugel, W.J.M. 1987, Nat 329, 604
- Chambers K. C., Miley G., van Breugel W.J. M., et al. 1996, ApJS, 106, 247
- Cimatti A., di Serego Alighieri S., Fosbury R., Salvati M. S., Taylor D. 1993, MNRAS, 264, 421
- Cimatti A., de Serego Alighieri S., Field, G.B., Fosbury, R.A.E. 1994, ApJ, 422, 562
- Cimatti A., di Serego Alighieri S., Vernet J., Cohen, M., Fosbury R.A.E. 1998, ApJ, 499, L21
- Colina L., Rieke M. J. 1997, "The 1997 HST Calibration Workshop with a new generation of instruments", S. Casertano, R. Jedrzejewski, C.D. Keyes, M. Stevens. edt Baltimore, MD, p. 18
- Daly R. A. 1990, ApJ, 355, 416
- Dey A., Cimatti A., van Breugel W., Antonucci R., Spinrad, H. 1996, ApJ, 465, 157
- Dey A., van Breugel W., Vacca W., Antonucci R. 1997, ApJ, 490, 698
- de Young D. S. 1989, ApJ, 342, L59
- di Serego Alighieri S., Fosbury R. A. E., Tadhunter P. Q. C. 1989, Nat 341, 307
- Dickson R., Tadhunter C., Shaw M., Clarck N., Morganti R. 1995, MNRAS, 273, L29
- Dubinski J. 1998, ApJ, 502, 141

- Eales S. A. 1992, ApJ, 397, 49
- Eales S.A., Rawlings S. 1990, MNRAS, 243, 1P
- Eales S. A., Rawlings S. 1993, ApJ, 411, 67
- Eales S.A., Rawlings, S. 1996, ApJ, 460, 68
- Eales S., Rawlings S. , Law-Green D., Gotter G., Lacy M. 1997, MNRAS, 291, 593
- Eisenhardt, P. and Chokshi, A. 1990, ApJ, 351, L9
- Elias, J. H., Frogel, J. A., Hyland, A. R. and Jones, T. J. 1983, AJ, 88, 1027
- Graham J.R., Matthews K., Soifer, B.T. et al. 1994, ApJ, 420, L5
- Giavalisco M., Steidel C., Macchetto F. 1996, ApJ, 189, 470
- HST Data Handbook, Version 2.0, December 1995, C. Leitherer ed.
- Kapahi V.K., Athreya R.M., van Breugel W., McCarthy P.J., Subrahmanya C.R. 1998, ApJS, 118, 275
- Lacy M., Rawlings S. 1996, MNRAS, 280, 888
- Le Fèvre O. L., Deltorn J., Crampton D., Dickinson M. 1996, ApJ, 471, L11
- Lilly S., 1988, ApJ, 333, 161
- McCarthy P. J.: 1993a, ARA&A, 31, 639
- McCarthy P. J., 1993b, PASP, 105, 105
- McCarthy P., van Breugel W., Spinrad H., Djorgovski S. 1987, ApJ, 321, L29
- McCarthy P., Kaphai V., van Breugel W., Subrahmanya, C.R. 1990, AJ, 100 1014
- McCarthy P.,van Breugel W., Kaphai V., Subrahmanya, C. R. 1991, AJ, 102, 522
- McCarthy P. J., Persson S. E., West S. C., 1992, ApJ, 386, 52
- McCarthy P., Kaphai V., van Breugel W. et al. 1996, ApJS, 107, 19
- McLeod, B. A. 1997, "The 1997 HST Calibration Workshop with a new generation of instruments" S. Casertano, R. Jedrzejewski, C.D. Keyes, and M. Stevens ed. Baltimore, MD, p. 281.

- McLure R.J., Dunlop J.S. 2000, MNRAS, in press
- Papadopoulos P.P., Rottgering H.J.A., van der Werf P. P., Guilloteau, S. et al. 2000, ApJ, 528, 626
- Pentericci L., Kurk, J.D., Rottgering H.J.A. et al. 2000a, A&A, 361L, 25
- Pentericci L., Rottgering H., Miley G., Carilli C., McCarthy P. 1997, A&A, 500, 580
- Pentericci L., Röttgering H., Miley G.K., et al. 1998, ApJ504, 139
- Pentericci L., Röttgering H., Miley G.K., et al. 1999, A&A, 341, 329
- Pentericci L., van Reveen W., Carilli C.L., Rottgering H., Miley G. 2000b, A&AS, 145 121
- Rigler M., Lilly S. 1994, ApJ, 427 79L
- Roche N., Eales S., Hippelein H. 1998a, MNRAS, 295, 946
- Röttgering H. J. A., West M., Miley G., Chambers K. 1996, A&A, 307, 376
- Röttgering H. J. A., Lacy, M. Miley G., Chambers K., Sauders R. 1994, A&A, 108,
- Rush B., McCarthy P.J, Athreya R.M., Persson S. 1997, ApJ, 163, 484
- Schombert J.M. 1987, ApJS, 64, 643
- Schombert J.M., 1988, ApJ, 328, 475
- Steidel C. C., Giavalisco M., Pettini M., Dickinson M., Adelberger K. L. 1996, ApJ, 462, 17
- Scarrott S. M., Rolph C. D., Tadhunter C. N., 1990, MNRAS, 243, 5P
- Tadhunter C. N., Scarrott S., Draper P., Rolph C., 1992, MNRAS, 256, 53p
- van Breugel W.J.M, Stanford S.A., Spinrad H., Stern D., Graham J.R. 1998, ApJ, 502, 614
- van Breugel W., de Breuck C., Röttgering H., Miley G.K. and Stanford, A. 1999, Looking Deep in the Southern Sky, 236
- van Ojik R., Röttgering H., Miley G., et al., 1994, A&A, 289, 54
- van Ojik, R., Roettgering, H. J. A., Carilli, C. L. et al. 1996, A&A, 313, 25
- van Ojik R., Rottgering H.J.A., Miley G.K., Hunstead R.W. 1997, A&A, 317, 358
- West M. 1994,MNRAS, 268, 79

Yan, L., McCarthy, P.J., Storrie-Lombardi, L.J. and Weymann, R.J. 1998, ApJ, 503, L19

Wilson, A. S. & Tsvetanov, Z. I. 1994, AJ, 107, 1227

Table 1. Properties of the radio sources.

Source (1)	z (2)	RA (3)	Decl (4)	$S_{4.7}$ (5)	$\alpha_{8.2}^{4.7}$ (6)	Size (7)	Morphology (8)
MRC 0140–257	2.64	01h42m41.16s	-25d30m34.1s	47	1.3	4.2	double
MRC 0152–209	1.89	01h54m55.77s	-20d40m26.3s	115	1.9	1.6	one-sided
MRC 0156–252	2.09	01h58m33.45s	-24d59m30.2s	112	1.1	8.3	double,distorted
USS 0211–122	2.34	02h14m17.37s	-11d58m46.7s	54	1.5	17.0	double
MRC 0316–257	3.13	03h18m12.06s	-25d35m09.7s	101	1.3	7.6	double
MRC 0324–228	1.89	03h27m04.44s	-22d39m42.6s	131	1.2 ^a	9.7	double, no core
MRC 0350–279	1.90	03h52m51.64s	-27d49m22.6s	86	1.2 ^a	≤ 0.6	unresolved
MRC 0406–244	2.44	04h08m51.44s	-24d18m16.7s	108	1.3	10.0	double
MRC 0943–242	2.93	09h45m32.79s	-24d28m49.8s	55	1.8	3.9	double,no core
MRC 1017–220	1.77	10h19m49.05s	-22d19m58.0s	261	1.1	≤ 0.6	unresolved
MRC 1138–262	2.16	11h40m48.25s	-26d29m10.1s	153	1.8	15.8	double,distorted
USS 1410–001	2.33	14h13m15.13s	-00d22m59.6s	57	1.3	24.0	double
USS 1707+105	2.35	17h10m06.85s	+10d31m09.0s	64	1.2	22.5	double,no core
MRC 2025–218	2.63	20h27m59.45s	-21d40m57.1s	95	1.1	5.1	double,distorted
MRC 2048–272	2.06	20h51m03.37s	-27d03m04.6s	115	1.6	8.3	double
MRC 2104–242	2.49	21h06m58.16s	-24d05m11.3s	107	1.0	24	double
USS 2202+128	2.70	22h05m14.27s	+13d05m33.7s	52	1.5	4.2	double
MRC 2224–273	1.68	22h27m43.26s	-27d05m01.7s	60	1.6	≤ 0.6	unresolved
USS 2349+280	2.89	23h51m59.08s	+29d10m28.9s	34	1.6 ^b	15.2	double

^a Spectral index between 4.7 GHz and 408 MHz

^bSpectral index between 4.7 GHz and 1.4 GHz

Note. — (1) 1950IAU name of the radio galaxy; (2) redshift; (3) and (4) position of the radio core (J2000 coordinates); (5) total flux and 4.7 GHz; (6) total spectral index between 4.7 and 8.2 GHz; (7) total extension in arcsecond; (8) radio morphology at 8.2 GHz

Table 2. NICMOS observations .

Source (1)	Date (2)	N (3)	$\mu_{(3\sigma)}$ (4)	T_{exp} (5)	Filter (6)	λ_r (7)	Cont. lines (8)	%flux (9)
MRC 0140–257	17/10/97	4	25.00	10195	F160W	3850-4950	H β	1
MRC 0152–209	26/12/97	4	24.48	10259	F160W	4840-6230	[OIII]	6
MRC 0156–252	28/09/97	4	24.89	9232	F160W	4530-5830	[OIII],H β	5
USS 0211–122	19/10/97	4	24.65	10195	F160W	4190-5390	[OIII],H β	3
MRC 0316–257	17/10/97	4	24.76	10195	F160W	3390-4360	[OII]	10
MRC 0324–228	22/06/97	2	24.50	5065	F165M	5540-6230	–	–
MRC 0350–279	18/10/97	4	24.63	10195	F160W	4830-6210	[OIII]	–
MRC 0406–244	11/08/97	5	24.84	12824	F160W	4070-5230	[OIII],H β	17
MRC 0943–242	12/06/97	3	24.55	7694	F160W	3560-4580	[OII]	7
MRC 1017–220	13/06/97	2	24.25	5065	F165M	5780-6500	[OI]	–
MRC 1138–262	27/11/97	5	24.57	12824	F160W	4430-5700	[OIII],H β	2
USS 1410–001	07/01/98	4	24.76	10195	F160W	4200-5410	[OIII],H β	9
USS 1707+105	24/10/97	4	25.01	10195	F160W	4180-5370	[OIII],H β	2
MRC 2025–218	09/09/97	4	24.64	10259	F160W	3860-4960	H β	1
MRC 2048–272	23/10/97	4	24.65	10259	F160W	4580-5880	[OIII],H β	–
MRC 2104–242	24/10/97	4	24.61	10259	F160W	4010-5160	[OIII],H β	26
USS 2202+128	21/06/97	2	24.25	5065	F165M	4320-4860	H β	2
MRC 2224–273	11/11/97	4	24.68	10259	F160W	5220-6720	H α ,[OI]	28
USS 2349+280	24/11/97	4	24.78	10195	F160W	3600-4630	[OII]	2

Note. — (1) 1950IAU name of the radio galaxy; (2) observation date; (3) number of orbits;(4) limiting surface brightness in H magnitudes; (5) total exposure time (seconds); (6) filter used; (7) restframe wavelength range covered by the observations; (8) emission lines falling in the continuum band;(9) estimated percentage of line flux in the total emission measured within a 4'' circular aperture.

Table 3. Ground based observations log

Galaxy (1)	Telescope (2)	Date (3)	Band (4)	λ_0 (5)	T_{exp} (6)	Res. (7)	Ref (8)
MRC 0156–252	du Pont 2.5m	27/10/89	Ly α	3700/50	8100	1.5''	1
	du Pont 2.5m	15/11/96	K $_s$	2.2 μ	4770	0.9''	1
	du Pont 2.5m	9/09/91	I	8100	1800	0.9''	1
MRC 0406–244	du Pont 2.5m	17/02/96	Ly α	4200/100	9000	1.1''	2
	du Pont 2.5m	19/11/96	K $_s$	2.2 μ	9030	0.9''	2
	du Pont 2.5m	8/09/91	I	8100	1300	0.9''	2
	NTT/EMMI	24/11/97	Spectr. Grat 3	4180	4800	2.8 \AA	1
MRC 2104–242	du Pont 2.5m	29/10/89	Ly α	4265/50	7800	1.4''	1
	du Pont 2.5m	9/09/91	r	6400	3100	0.7''	1
	NTT/EMMI	30/06/97	Spectr. Grat 3	4240	7200	2.8 \AA	1

Note. — (1) Radio galaxy; (2) Telescope used; (3) observation date ; (4) filter or grating used; (5) observed wavelength covered (in \AA); (6) total exposure time (in seconds); (7) resolution; (8) reference 1. This paper; 2. Rush et al. 1997

Table 4. Photometry

Galaxy	Comp.	Ap.	M_H	err
MRC 0140–257	main	4''	20.13	0.07
MRC 0152–209	main	4''	18.69	0.04
MRC 0156–252	A	4''	18.39	0.10
	B	2''	21.58	0.10
	C	2''	20.22	0.10
USS 0211–122	main	4''	19.64	0.04
MRC 0316–257	main	4''	20.23	0.05
MRC 0324–228	main	4''	19.93	0.03
MRC 0350–279	main	4''	20.26	0.10
MRC 0406–244	A	4''	18.91	0.04
	B	1''	21.36	0.10
	C	1''	21.23	0.10
	D	1''	21.62	0.10
	E	1''	22.67	0.10
MRC 0943–242	main	4''	19.77	0.08
MRC 1017–220	main	4''	18.28	0.05
MRC 1138–262	A	4''	18.04	0.03
	B	1''	23.13	0.20
	C1	1''	21.11	0.10
	C2	1''	22.07	0.10
	E	1''	23.48	0.20
	F	1''	22.04	0.10
	H	1''	21.68	0.10
USS 1410–001	main	4''	19.25	0.05
USS 1707+105	A	4''	20.15	0.04
	B	1''	23.50	0.20
	C	1''	22.30	0.10
	D	1''	22.65	0.10
	E	1''	22.63	0.10
MRC 2025–218	main	4''	18.94	0.04
MRC 2048–272	main	4''	20.18	0.04
MRC 2104–242	A	4''	19.91	0.10
	B	2''	21.18	0.10
USS 2202+128	main	4''	19.80	0.10
MRC 2224–273	main	4''	19.23	0.05
USS 2349+280	main	4''	19.94	0.05

Table 5. Parameters of the de Vaucouleurs fit

Galaxy	z	r_e arcsec	r_e kpc	μ_e H-mag arcsec ⁻²	χ^2/ν
MRC 0152–209	1.89	0.64	5.3	20.8	1.33
USS 0211–122	2.34	0.73	5.7	21.8	1.11
MRC 1707+105	2.35	1.62	12.7	23.7	1.06
MRC 2048–272	2.06	0.2	1.6	19.1	0.64
MRC 2224–273	1.68	0.2	1.7	18.6	1.12

Note. — (1) Radio galaxy; (2) redshift; (3) best fitting r_e in arcseconds; (4) best fitting r_e in kpc; (5) best fitting μ_e ; (6) reduced chi-squared

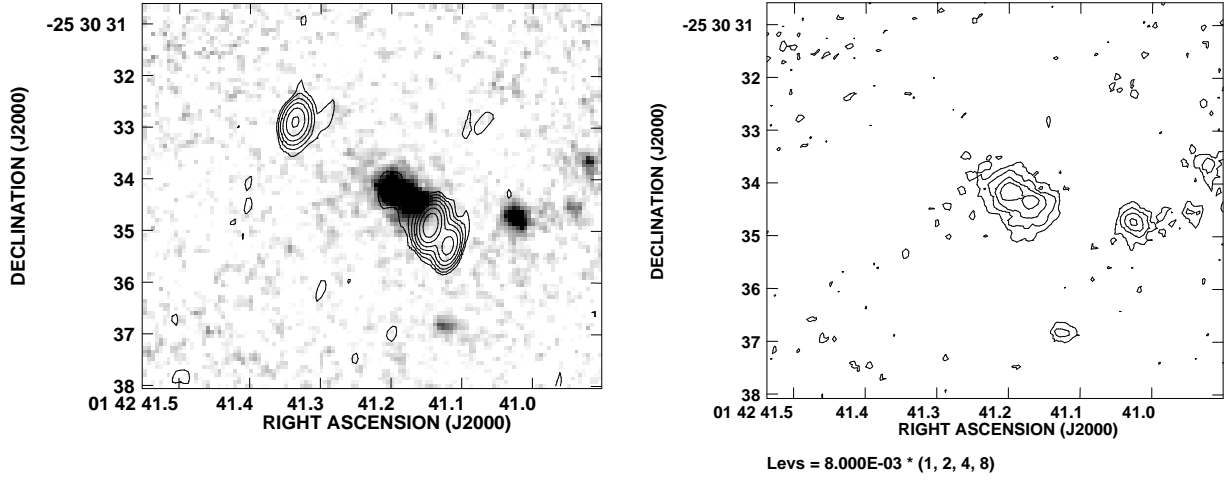


Fig. 1.— *Left*: A grey scale representation of the near infrared continuum emission of the radio galaxy MRC 0140–257 at $z = 2.64$ with contours from the VLA 8.2 GHz observations super-imposed. *Right*: Contour representation of the continuum emission. Contour levels of flux density at: $1, 2, 4, 8 \times 0.8 \cdot 10^{-2} \mu\text{Jy}$.

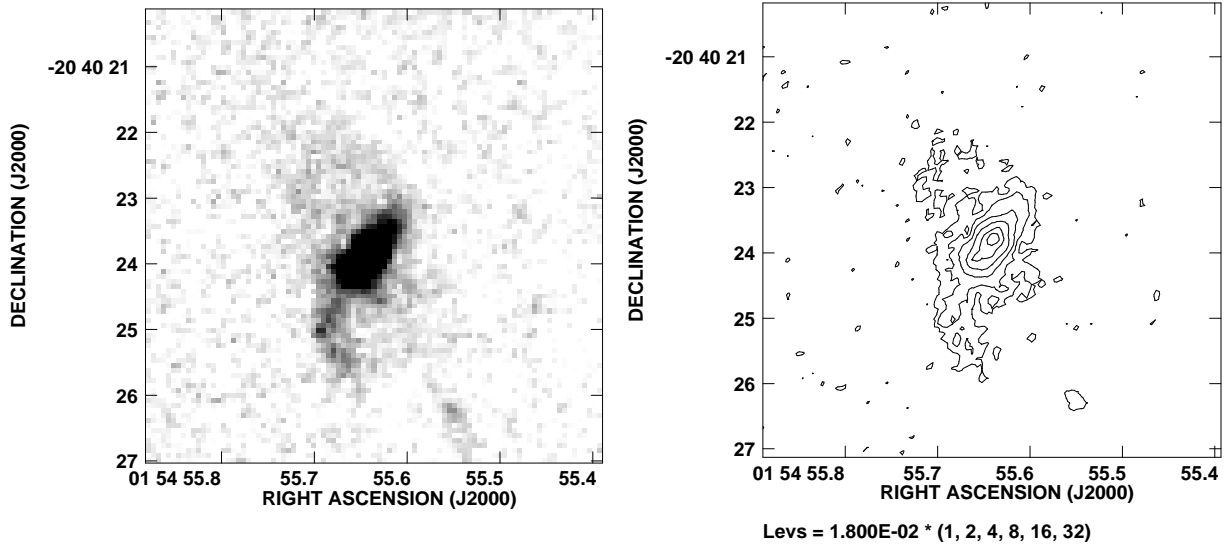


Fig. 2.— *Left*: A grey scale representation of the near infrared continuum emission of the radio galaxy MRC 0152–209 at $z = 1.89$. *Right*: Contour representation of the same image. Contour levels of flux density at: $1, 2, 4, 8, 16, 32 \times 1.8 \cdot 10^{-1} \mu\text{Jy}$.

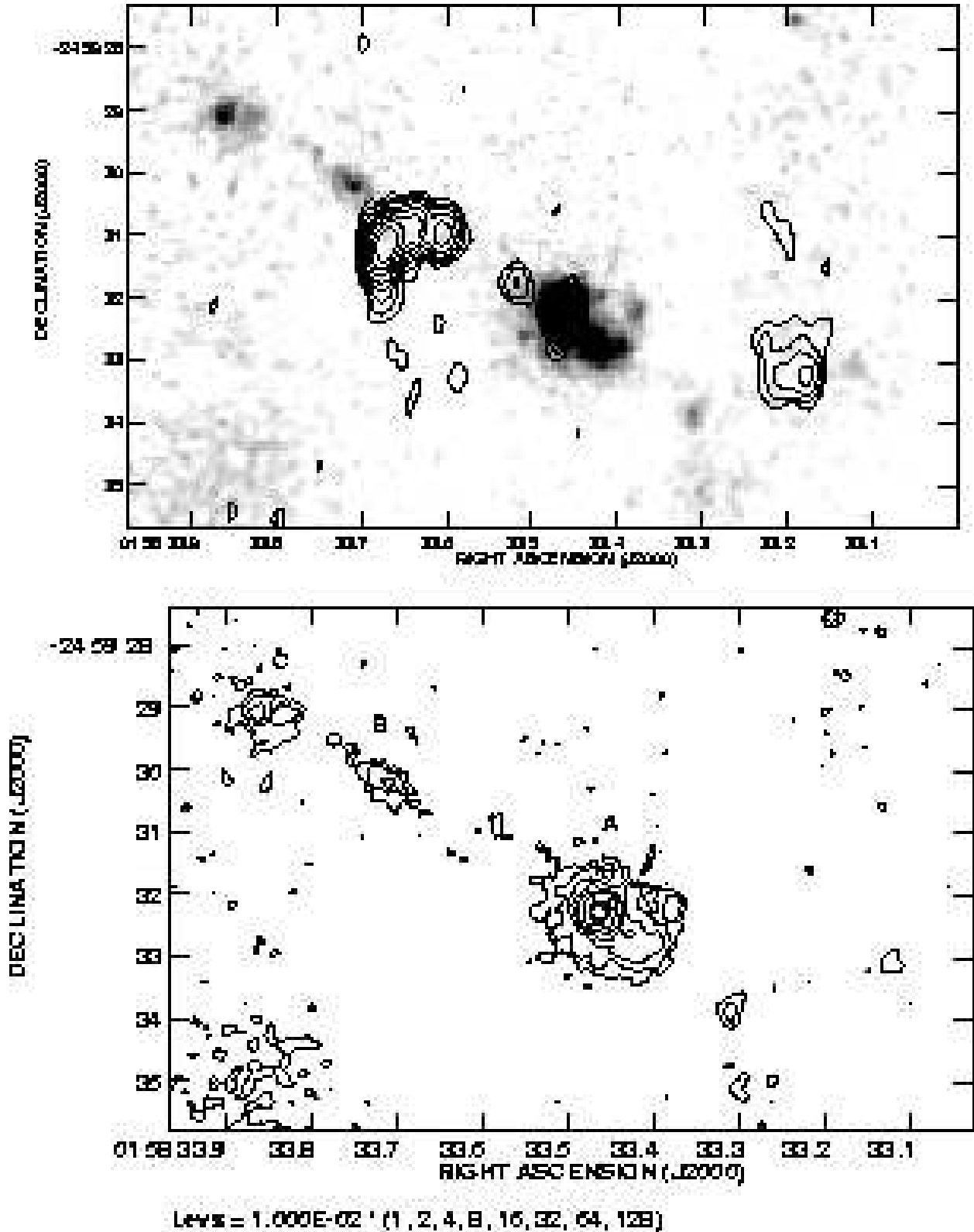


Fig. 3.— *Top panel:* A grey scale representation of the near infrared continuum emission of the radio galaxy MRC 0156–252 at $z = 2.09$ with contours from the VLA 8.2 GHz observations super-imposed. *Bottom panel:* Contour representation of the continuum emission. Contour representation of the same image. Contour levels of flux density at: 1,2,4,8,16,32,64,128 $\times 10^{-2} \mu\text{Jy}$.

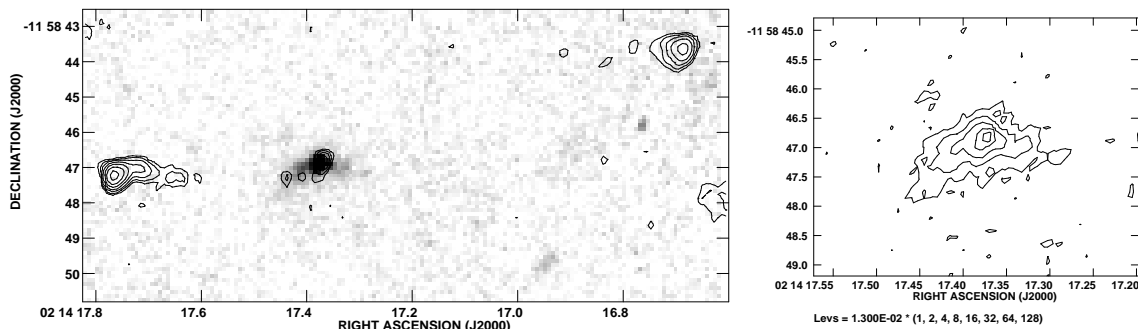


Fig. 4.— *Left*: A grey scale representation of the near infrared continuum emission of the radio galaxy USS 0211–122 at $z = 2.34$ with contours from the VLA 8.2 GHz observations super-imposed. *Right*: Contour representation of the continuum emission from the host galaxy. Contour levels of flux density at: $1, 2, 4, 8, 16 \times 1.3 \cdot 10^{-2} \mu\text{Jy}$.

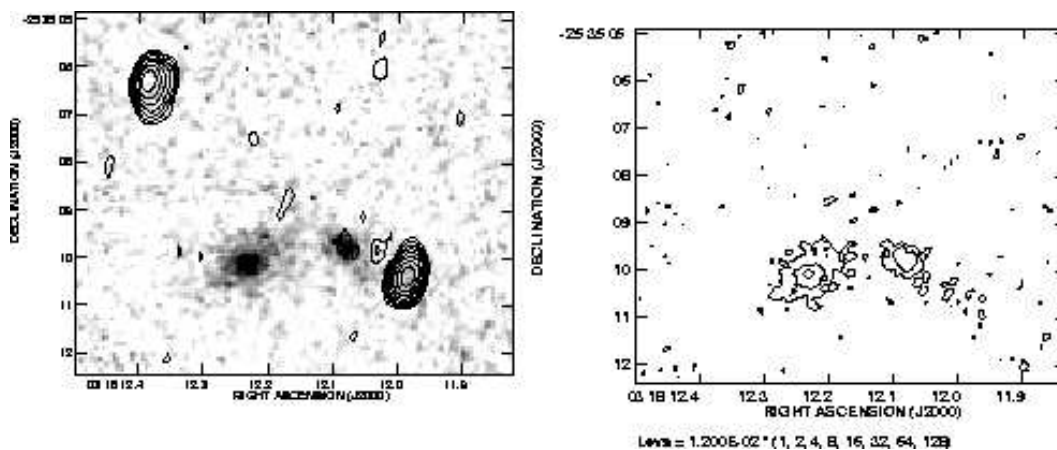


Fig. 5.— *Left*: A grey scale representation of the near infrared continuum emission of the radio galaxy MRC 0316–257 at $z = 3.13$ with contours from the VLA 8.2 GHz observations super-imposed. *Right*: Contour representation of the continuum emission. Contour levels of flux density at: $1, 2, 4 \times 1.2 \cdot 10^{-2} \mu\text{Jy}$.

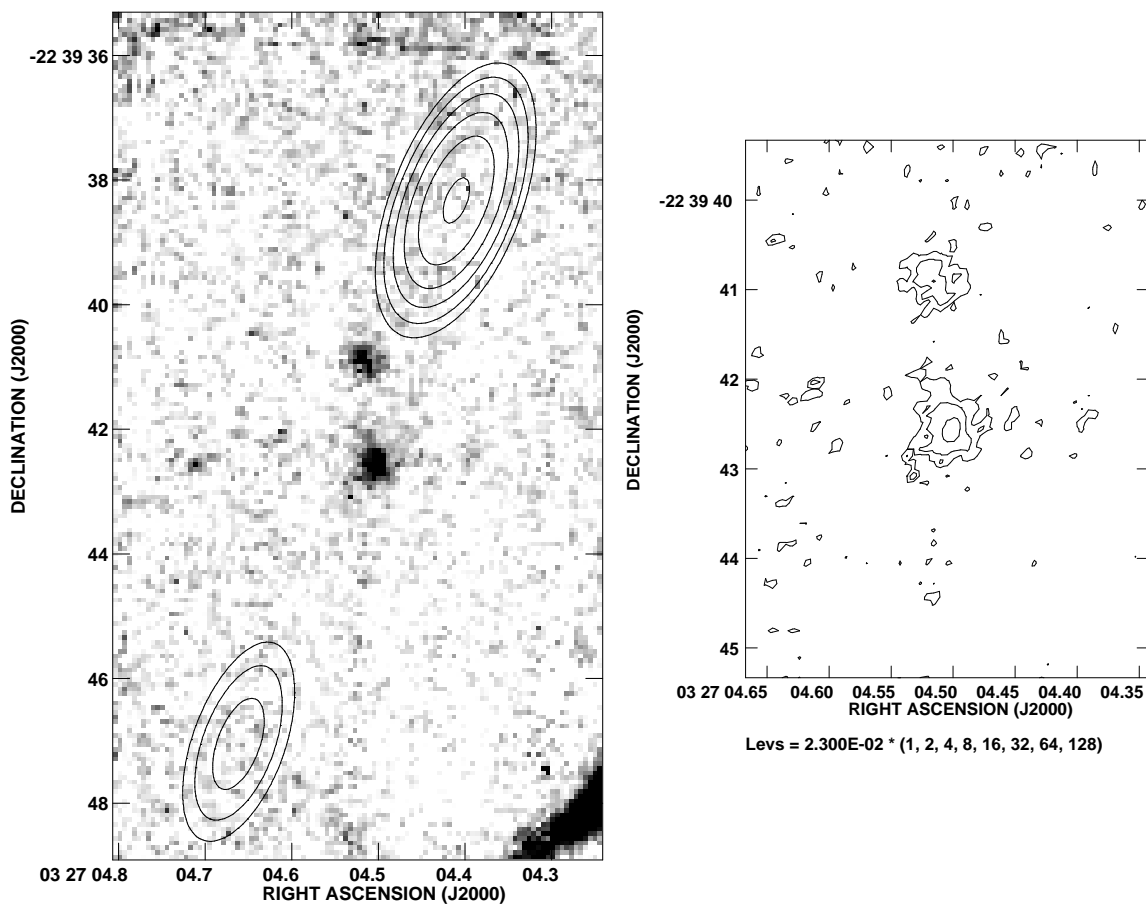


Fig. 6.— *Left*: A grey scale representation of the near infrared continuum emission of the radio galaxy MRC 0324–228 at $z = 1.89$ with contours from the VLA 4.5 GHz observations super-imposed. *Right*: Contour representation of the continuum emission from the two possible identifications of the host galaxy. Contour levels of flux density at: $1, 2, 4, 8 \times 1.3 \cdot 10^{-2} \mu\text{Jy}$.

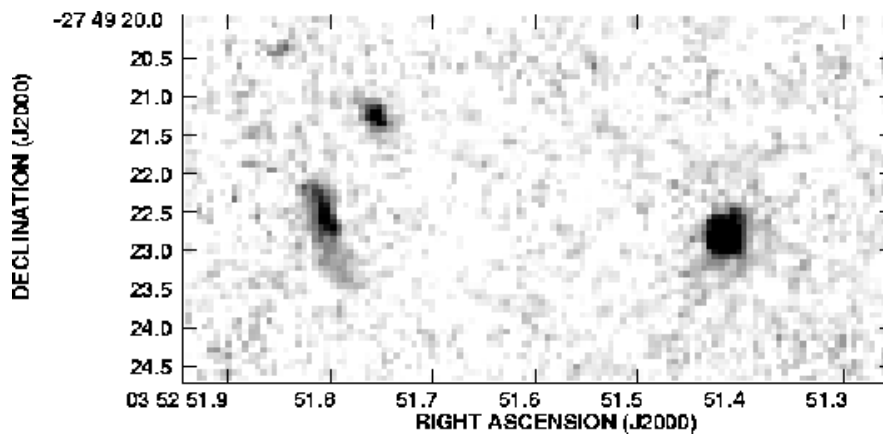


Fig. 7.— A grey scale representation of the near infrared continuum emission of the radio galaxy MRC 0350–279 at $z = 1.90$.

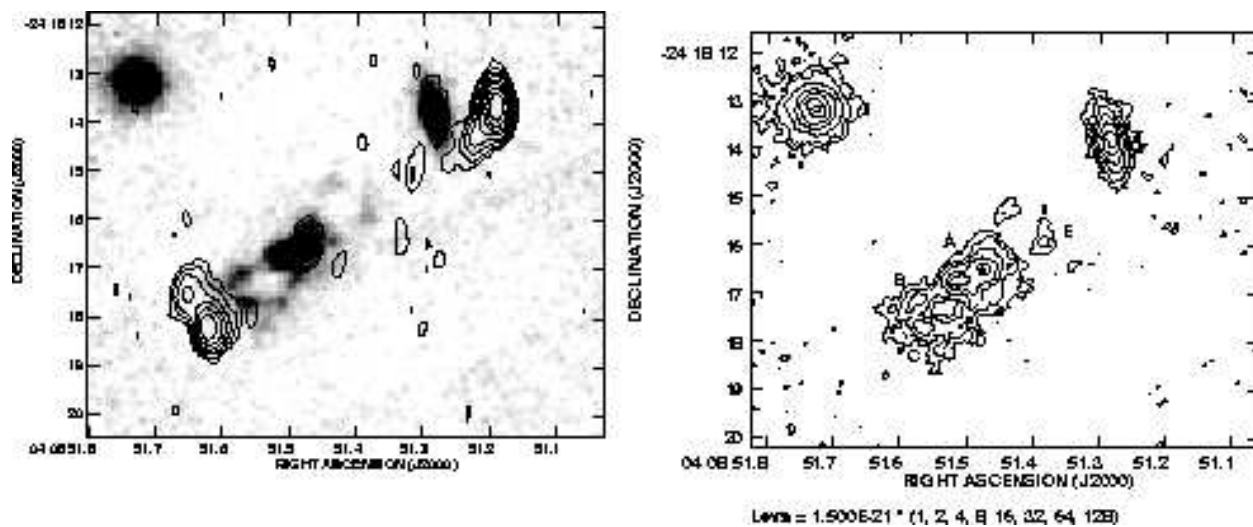


Fig. 8.— *Left*: A grey scale representation of the near infrared continuum emission of the radio galaxy MRC 0406–244 at $z = 2.44$ with contours from the VLA 8.2 GHz observations super-imposed. *Right*: Contour representation of the continuum emission. Contour levels of flux density at: $1, 2, 4, 8, 16, 32, 64, 128 \times 1.5 \cdot 10^{-21} \text{ erg sec}^{-1} \text{ cm}^{-2}$

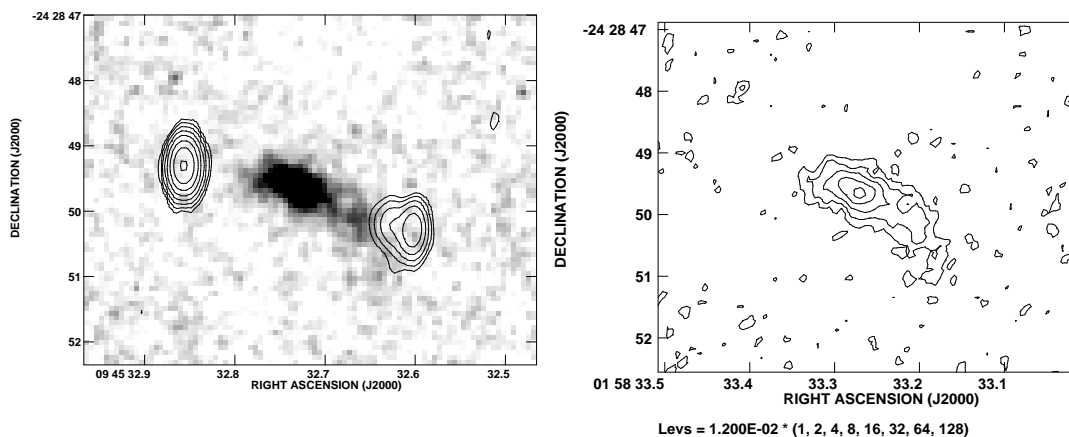


Fig. 9.— *Left*: A grey scale representation of the near infrared continuum emission of the radio galaxy MRC 0943–242 at $z = 2.93$ with contours from the VLA 8.2 GHz observations super-imposed. *Right*: Contour representation of the continuum emission. Contour levels of flux density at: $1, 2, 4, 8, 16 \times 1.2 \cdot 10^{-2} \mu\text{Jy}$.

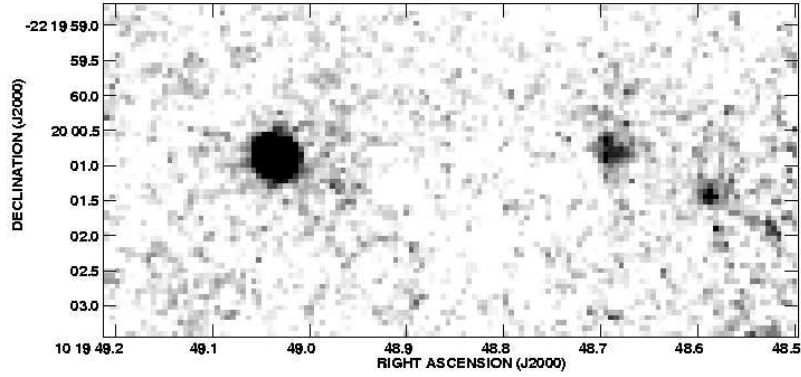


Fig. 10.— Grey scale representation of the near infrared continuum emission of the radio galaxy MRC 1017–220 at $z = 1.77$. The host of the radio source is the unresolved object to the east

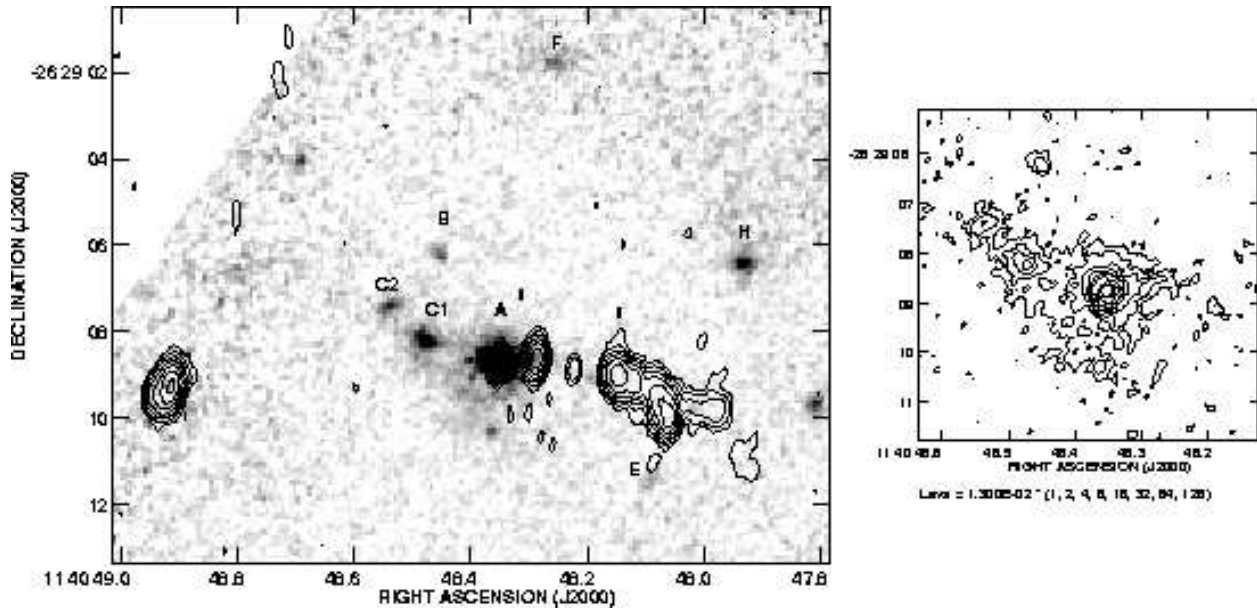


Fig. 11.— *Left*: A grey scale representation of the near infrared continuum emission of the radio galaxy MRC 1138–242 at $z = 2.16$ and its close companions, with contours from the VLA 8.2 GHz observations super-imposed. *Right*: Contour representation of the continuum emission from the central region. Contour levels of flux density at: $1, 2, 4, 8, 16, 32, 64, 128 \times 1.3 \cdot 10^{-2} \mu\text{Jy}$.

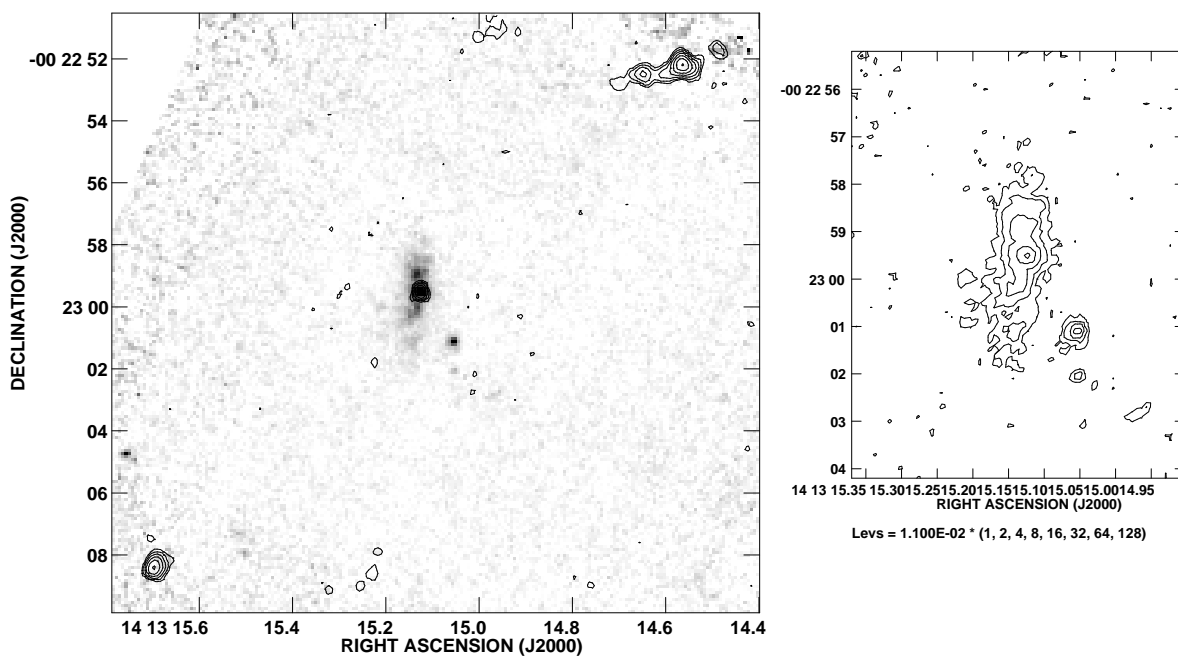


Fig. 12.— *Left*: Grey scale representation of the near infrared continuum emission of the radio galaxy USS 1410–001 at $z = 2.33$ with contours from the VLA 8.2 GHz observations super-imposed. *Right*: Contour representation of the continuum emission from the host galaxy. Contour levels of flux density at: $1, 2, 4, 8, 16 \times 1.1 \cdot 10^{-2} \mu\text{Jy}$.

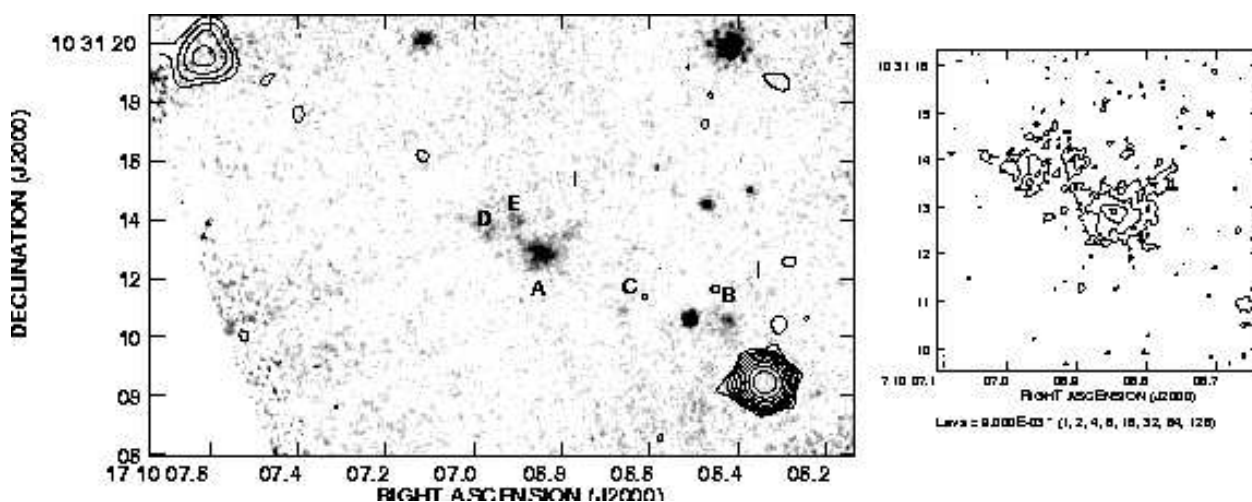


Fig. 13.— *Top panel*: Grey scale representation of the near infrared continuum emission of the radio galaxy USS 1707+105 at $z = 2.35$ and its close companions, with contours from the VLA 8.2 GHz observations super-imposed. *Bottom panel*: Contour representation of the continuum emission from the host galaxy. Contour levels of flux density at: $1, 2, 4, 8, 16 \times 0.9 \cdot 10^{-2} \mu\text{Jy}$.

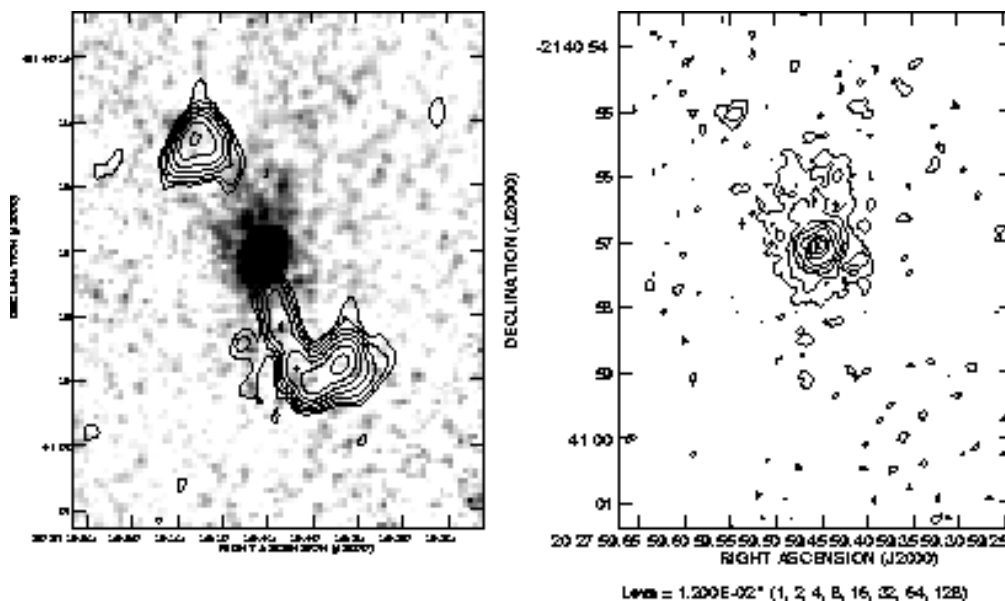


Fig. 14.— *Left*: Grey scale representation of the near infrared continuum emission of the radio galaxy MRC 2025–218 at $z = 2.63$ with contours from the VLA 8.2 GHz observations super-imposed. *Right*: Contour representation of the continuum emission. Contour levels of flux density at: $1, 2, 4, 8, 16, 32, 64, 128 \times 1.2 \cdot 10^{-2} \mu\text{Jy}$.

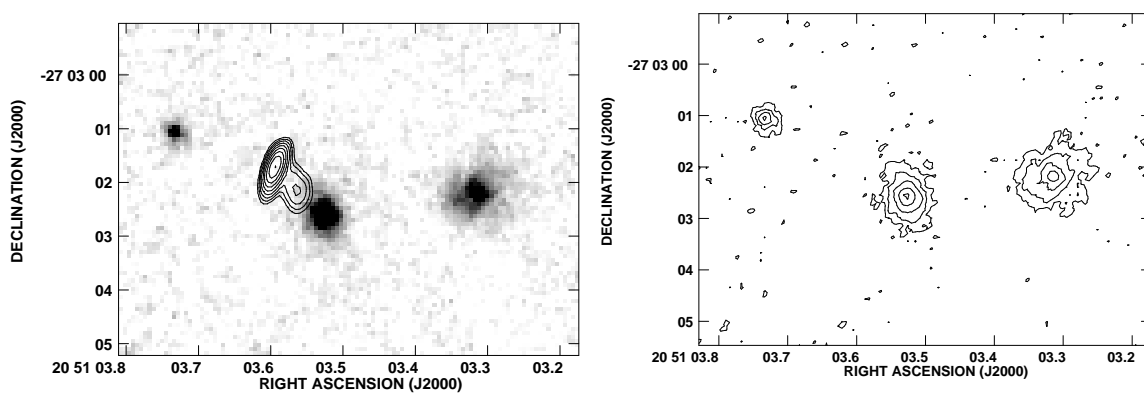


Fig. 15.— *Left*: Grey scale representation of the near infrared continuum emission of the radio galaxy MRC 2048–272 at $z = 2.06$ with contours from the VLA 8.2 GHz observations super-imposed. *Right*: Contour representation of the continuum emission. Contour levels of flux density at: $1, 2, 4, 8, 16 \times 1.4 \cdot 10^{-2} \mu\text{Jy}$.

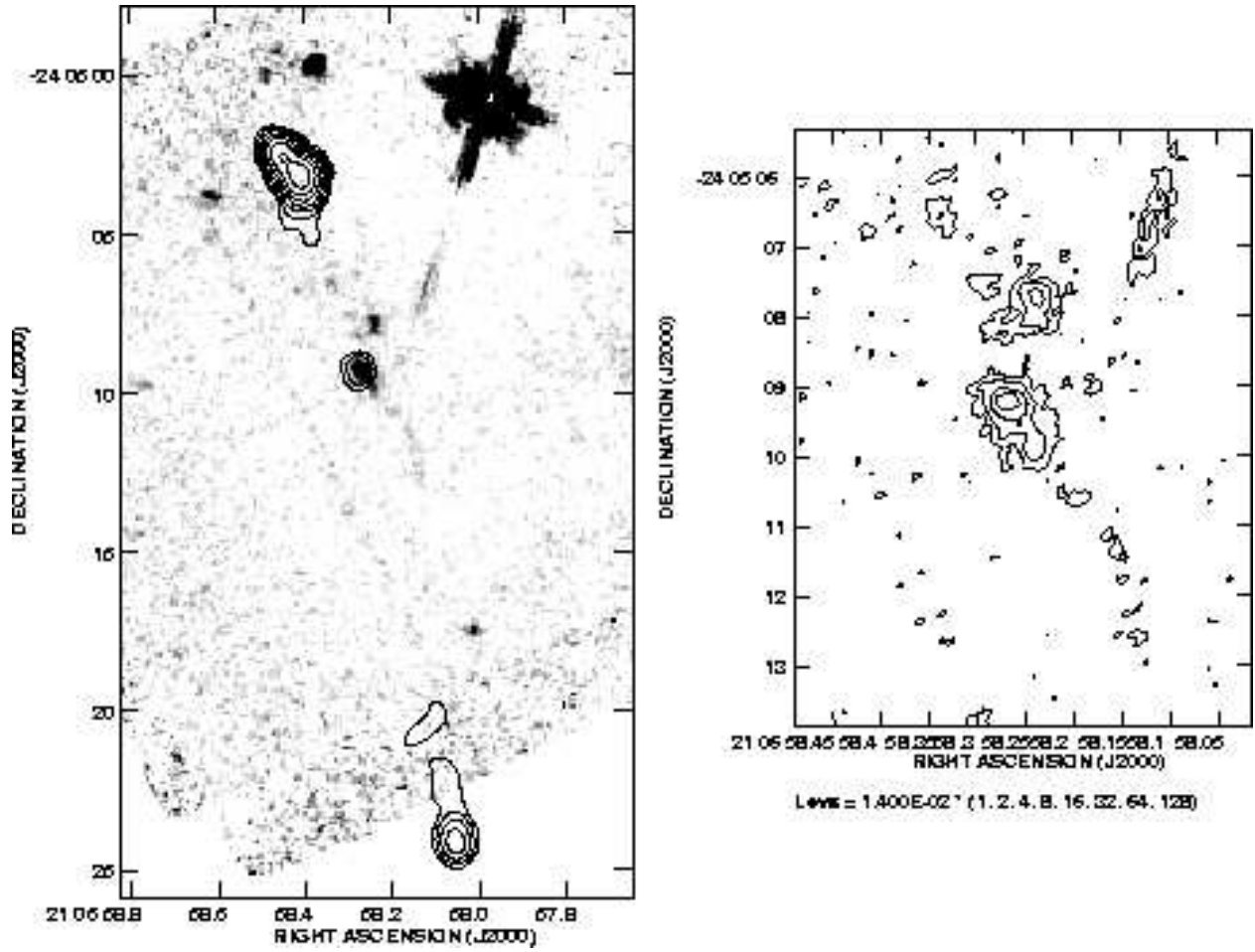


Fig. 16.— *Left*: Grey scale representation of the near infrared continuum emission of the radio galaxy MRC 2104–242 at $z = 2.49$ with contours from the VLA 8.2 GHz observations super-imposed. *Right*: Contour representation of the continuum emission from the central region. The elongated feature north-west of the galaxy core is a spike from the near by star. Contour levels of flux density at: $1, 2, 4, 8, 16 \times 1.4 \cdot 10^{-2} \mu\text{Jy}$.

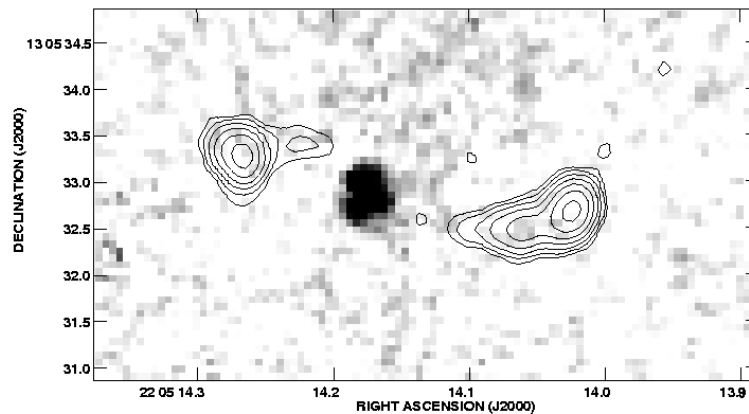


Fig. 17.— Grey scale representation of the near infrared continuum emission of the radio galaxy ICS 2202+128 at $z = 2.70$ with contours from the VLA 8.2 GHz observations super-

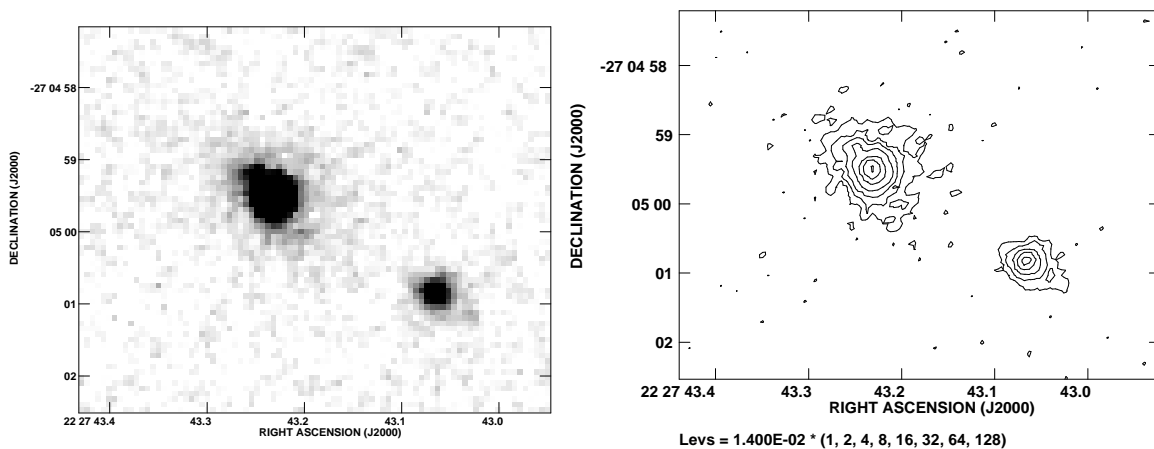


Fig. 18.— *Left*: Grey scale representation of the near infrared continuum emission of the radio galaxy MRC 2224–273 at $z = 1.68$. *Right*: Contour representation of the continuum emission. Contour levels of flux density at: $1, 2, 4, 8, 16, 32, 64 \times 1.4 \cdot 10^{-2} \mu\text{Jy}$.

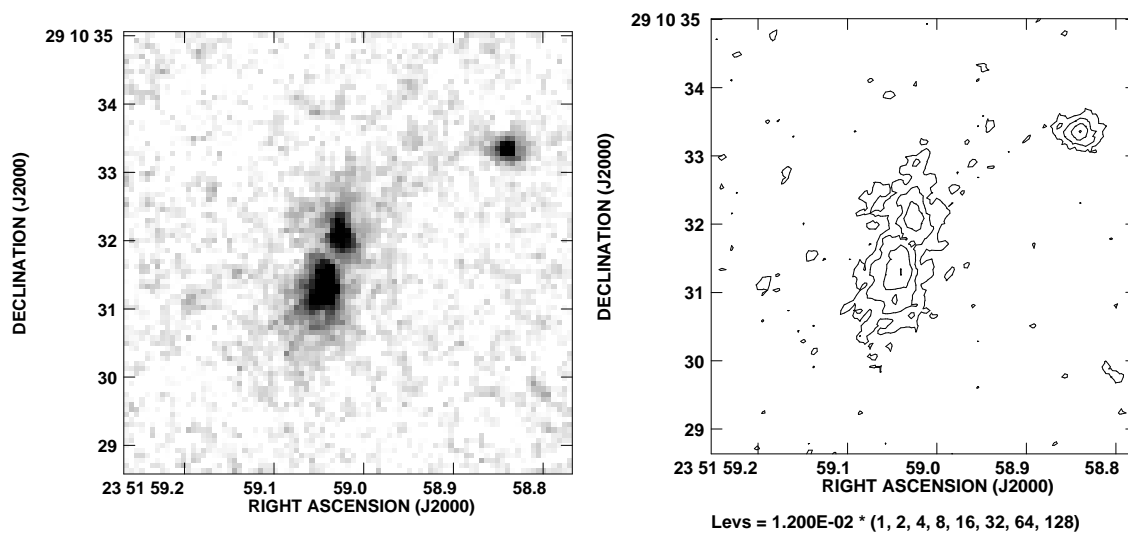


Fig. 19.— *Left*: Grey scale representation of the near infrared continuum emission of the radio galaxy USS 2349+280 at $z = 2.89$. *Right*: Contour representation of the continuum emission. Contour levels of flux density at: $1, 2, 4, 8 \times 1.2 \cdot 10^{-2} \mu\text{Jy}$.

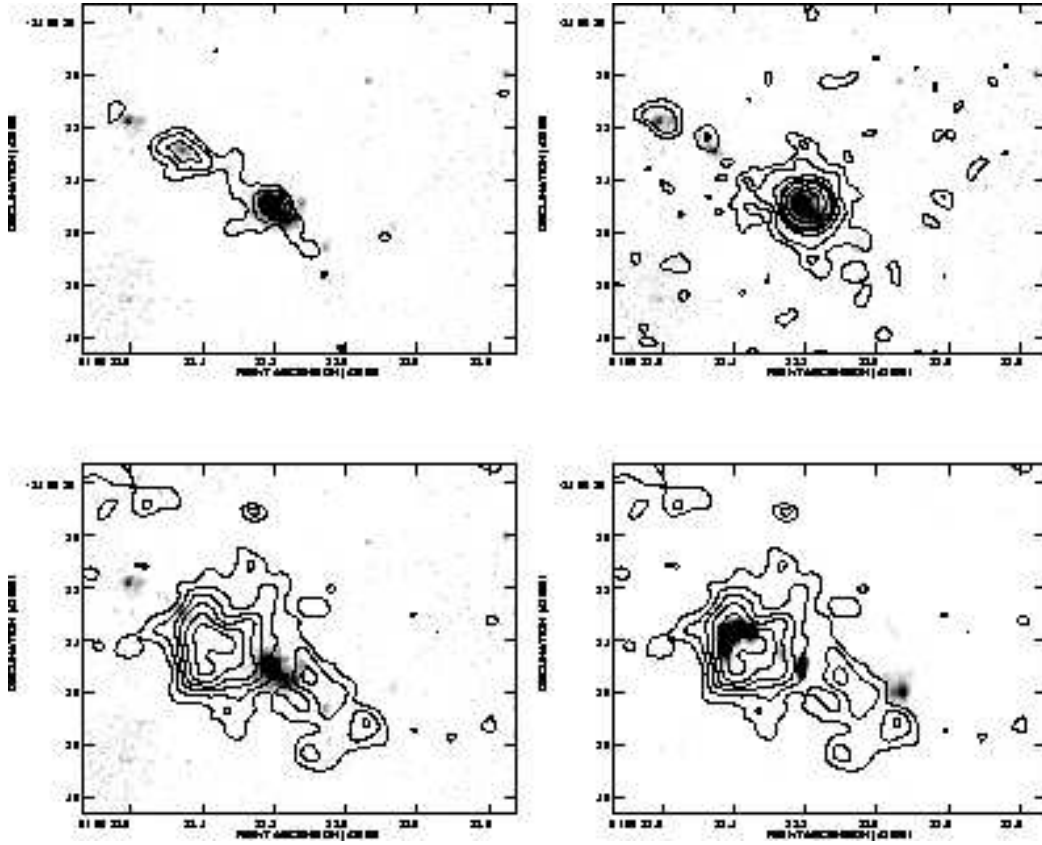


Fig. 20.— The NICMOS image of MRC 0156–252 in grey scale overlaid with contours representing the I-band emission (top left), K-band emission (top right) and narrow band Ly α emission (bottom left). The bottom right panel shows the 8.2 GHz radio emission in grey scale overlaid with contour of the narrow band Ly α emission

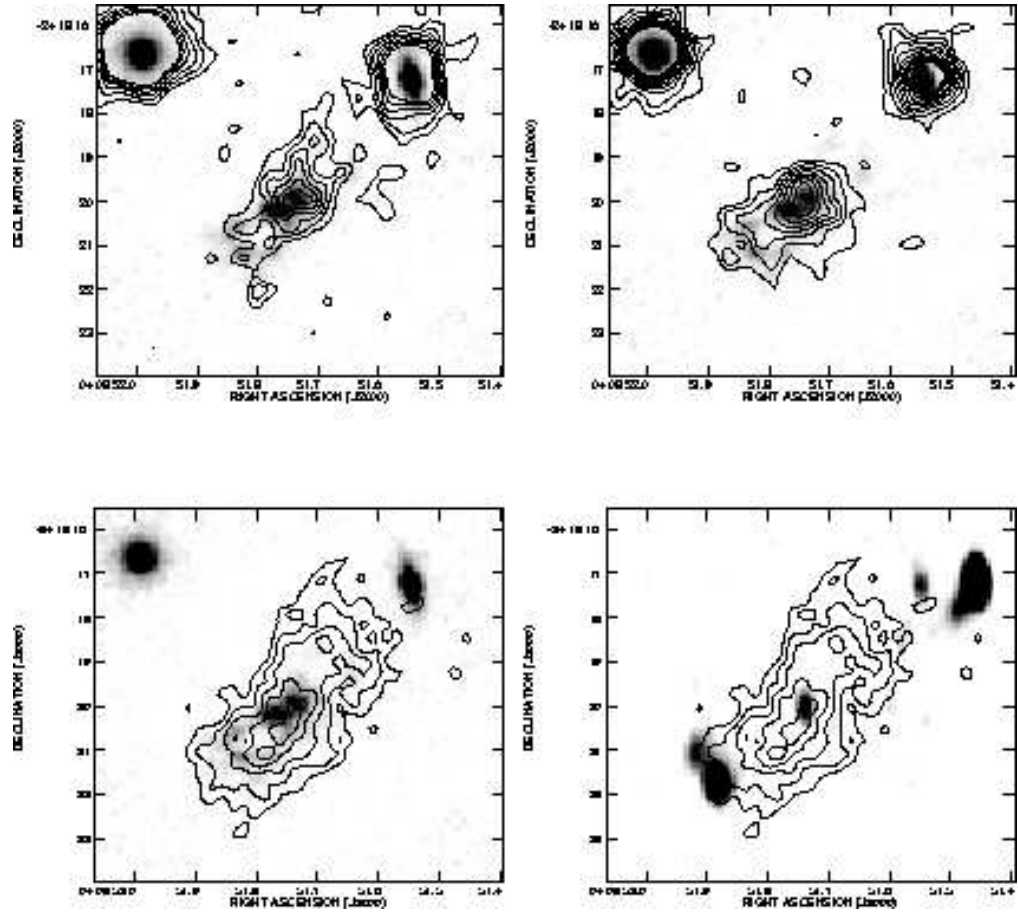


Fig. 21.— The NICMOS image of MRC 0406–244 in grey scale overlaid with contours representing the I-band emission (top left), K-band emission (top right) and narrow band Ly α emission (bottom left). The bottom right panel shows the 8.2 GHz radio emission in grey scale overlaid with contour of the narrow band Ly α emission.

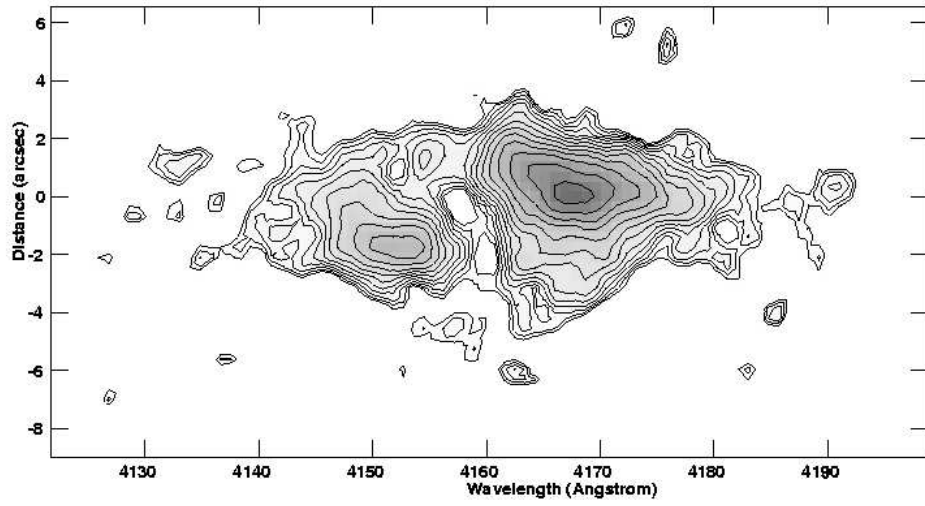


Fig. 22.— A high resolution spectrum of the Ly α emission line from MRC 0406–244, taken with the NTT, having a resolution of 2.8 \AA

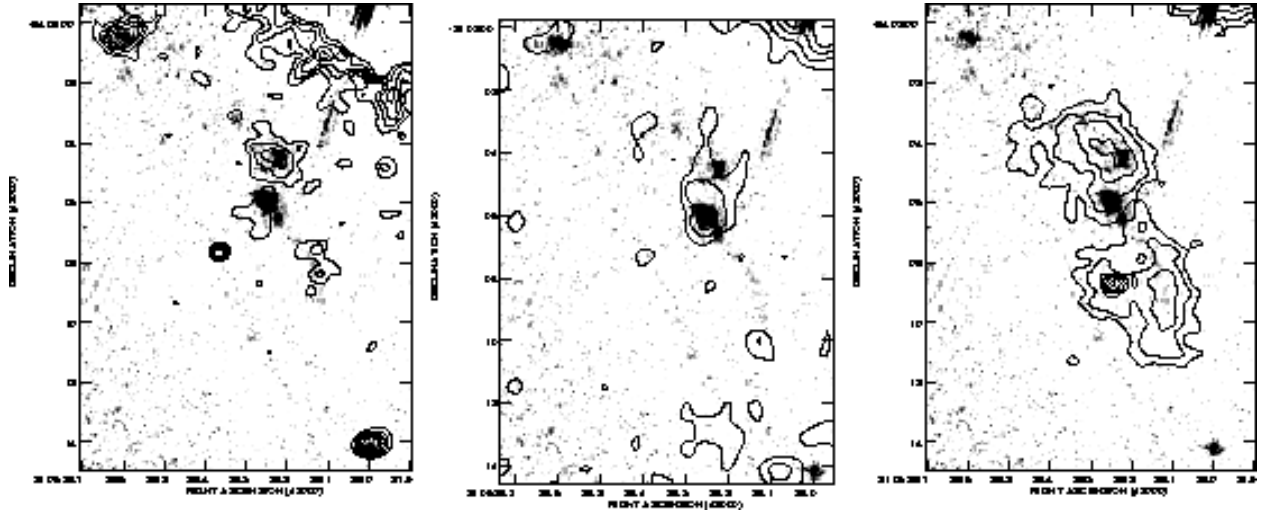


Fig. 23.— The NICMOS image of MRC 2104–242 in grey scale overlaid with contours of the R-band emission (left panel) K-band emission (central panel), and narrow band Ly α emission (right panel). The elongated feature on the top right of the images is a spike from a nearby bright star.

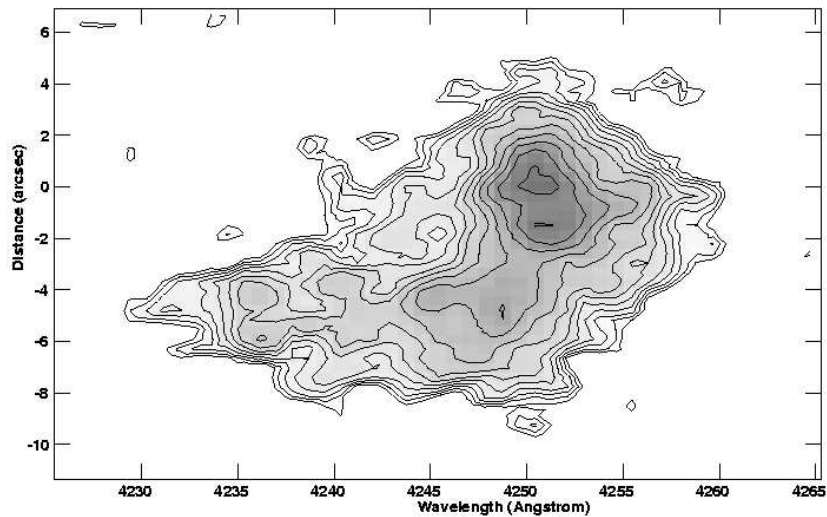


Fig. 24.— A high resolution spectrum of the Ly α emission line from MRC 2104–242, taken with the NTT, having a resolution of 2.8 \AA

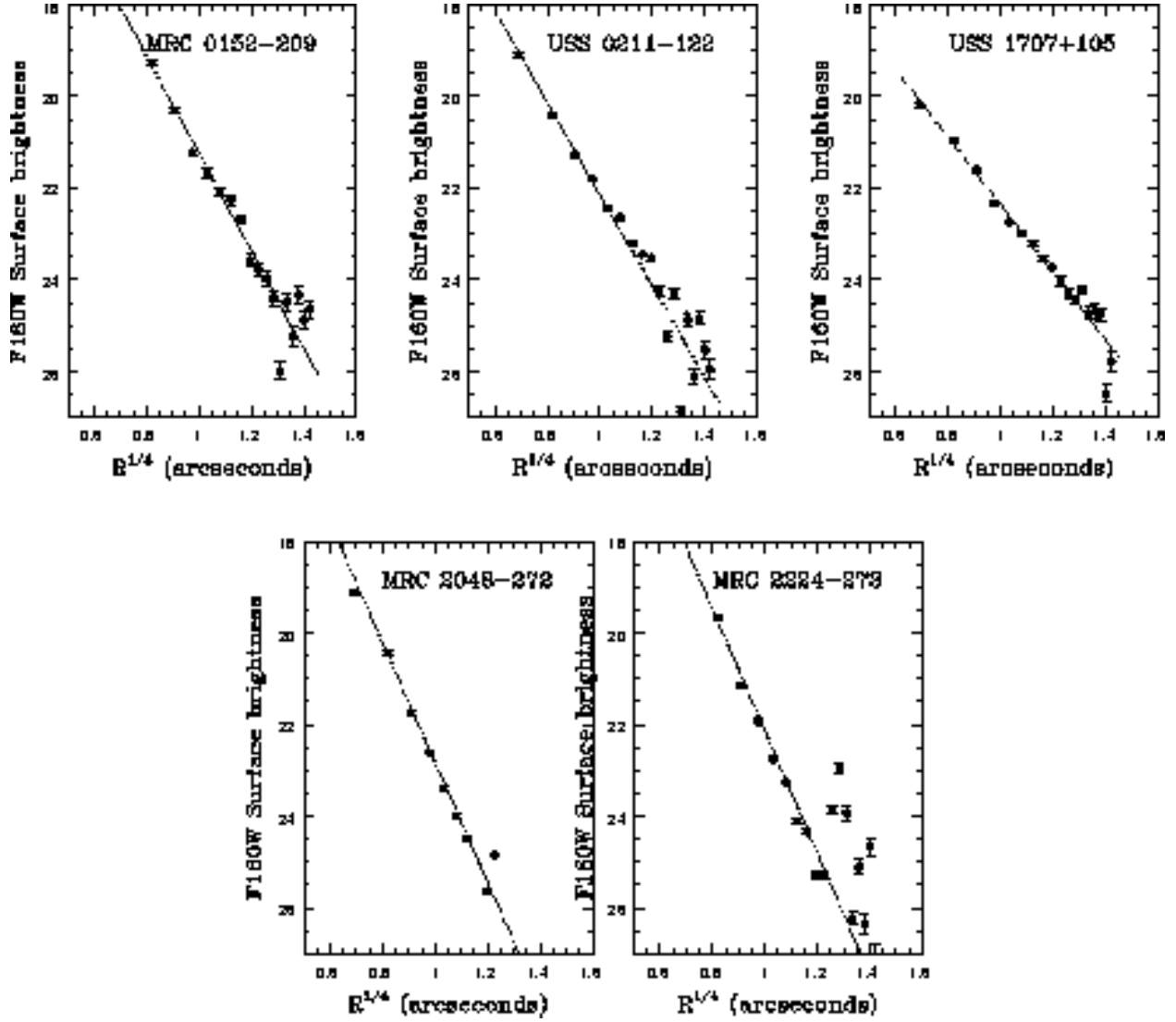


Fig. 25.— Surface brightness profiles for the 5 radio galaxies which are well represented by a de Vaucouleurs law: the filled circles are the data with their relative error bars, while the dotted lines are the best fit laws.

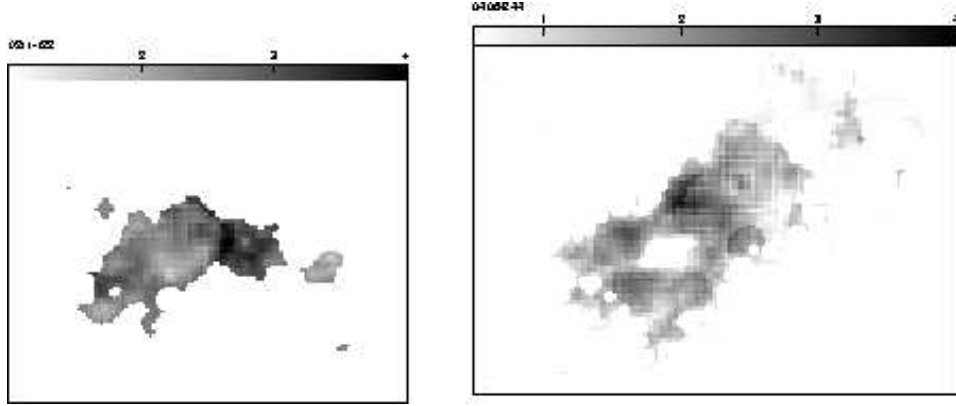


Fig. 26.— The optical to infrared spectral index distribution for the radio galaxies USS 0211–122 (left) and MRC 0406–244 (right). The bar on the top indicates the scale in each case

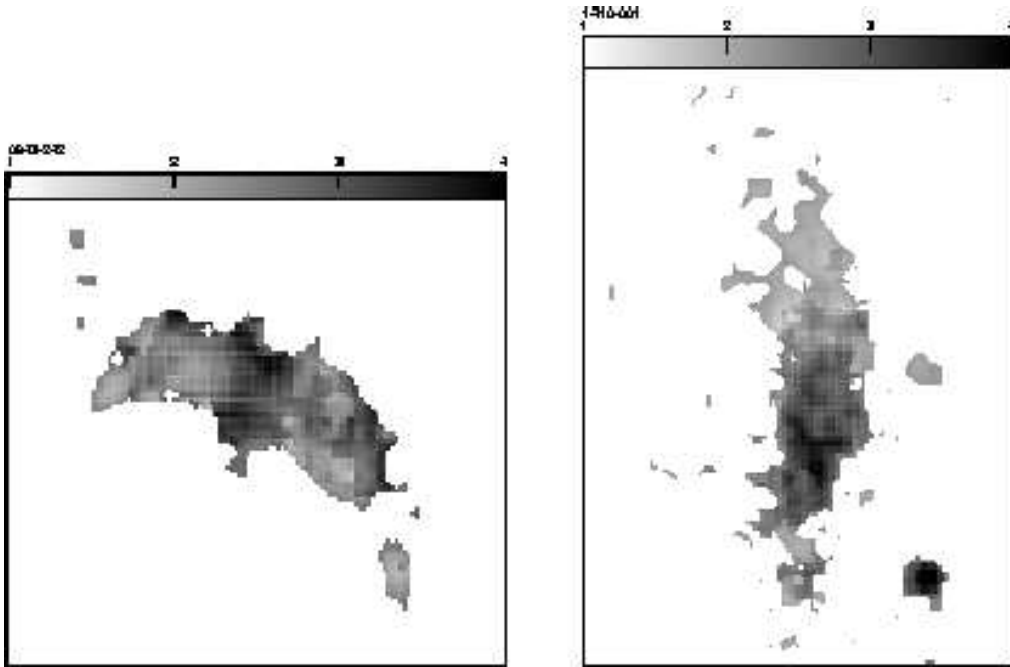


Fig. 27.— The optical to infrared spectral index distribution for the radio galaxies MRC 0943–242 (left) USS 1410–001 (right). The bar on the top indicates the scale in each case

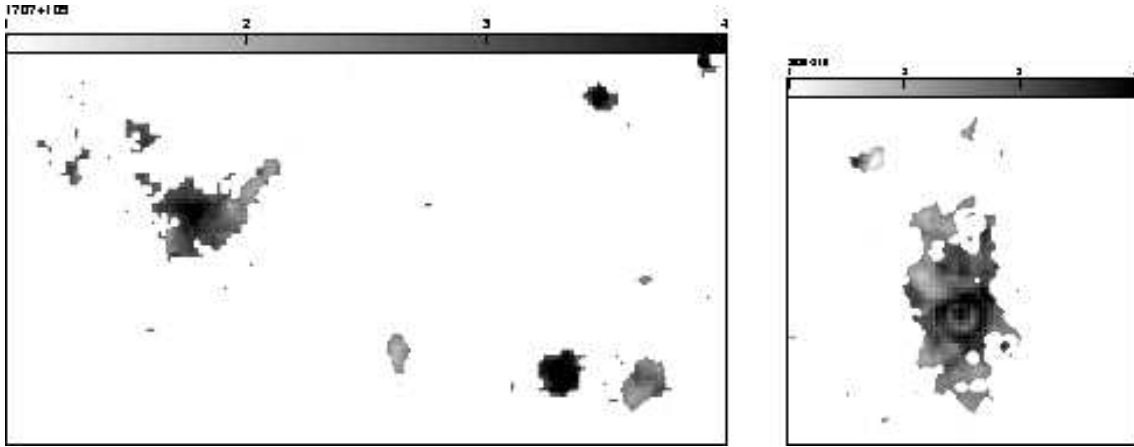


Fig. 28.— The optical to infrared spectral index distribution for the radio galaxy USS 1707+105 (left) and MRC 2025–218 (right). The bar on the top indicates the scale in each case

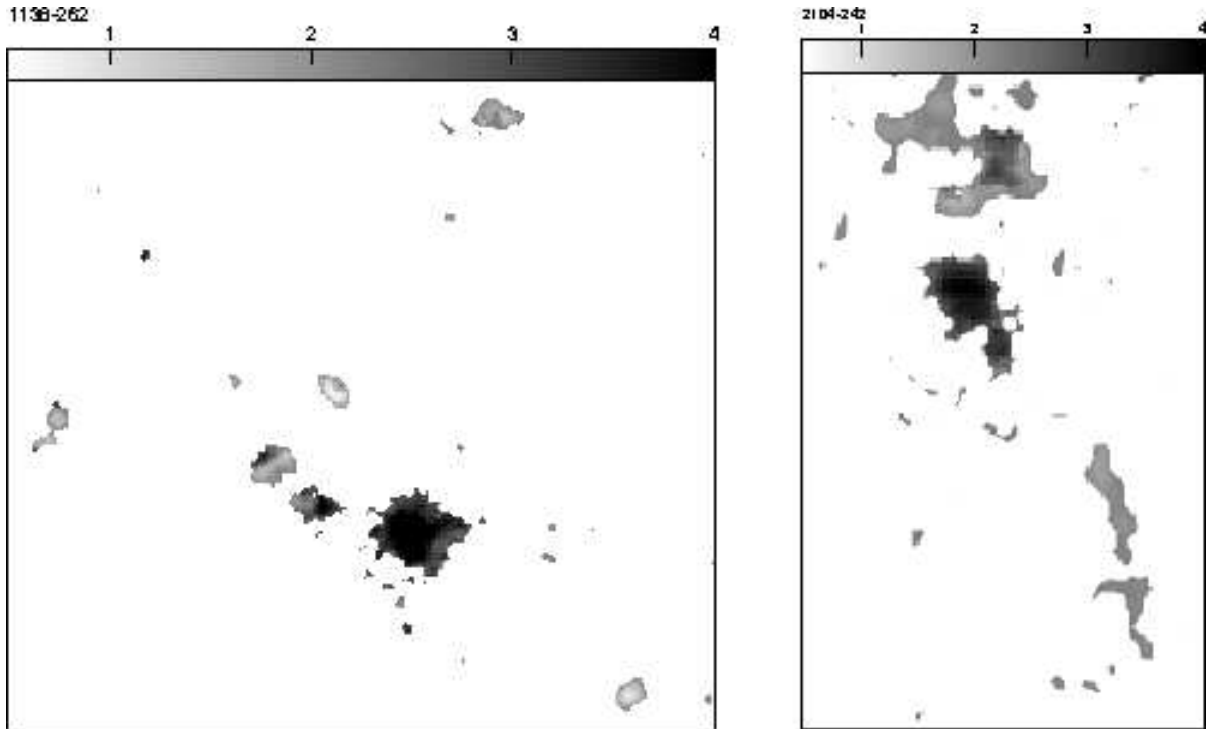


Fig. 29.— The optical to infrared spectral index distribution for the radio galaxies MRC 1138–262(left) and MRC 2025–218 (right). The bar on the top indicates the scale in each case. In these galaxies there is a strong contribution from a nuclear point source which influence the spectral indexes in the center.

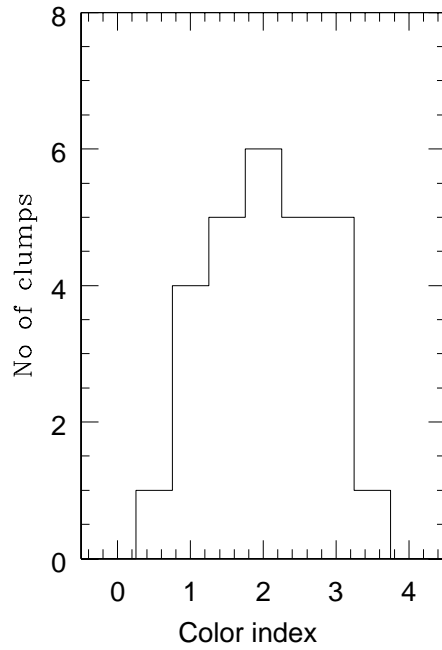


Fig. 30.— Distribution of the optical to infrared spectral indices of the components of the 4 clumpy radio galaxies, MRC 0406–244, MRC 1138–262, USS 1707+105 and MRC 2104–242.

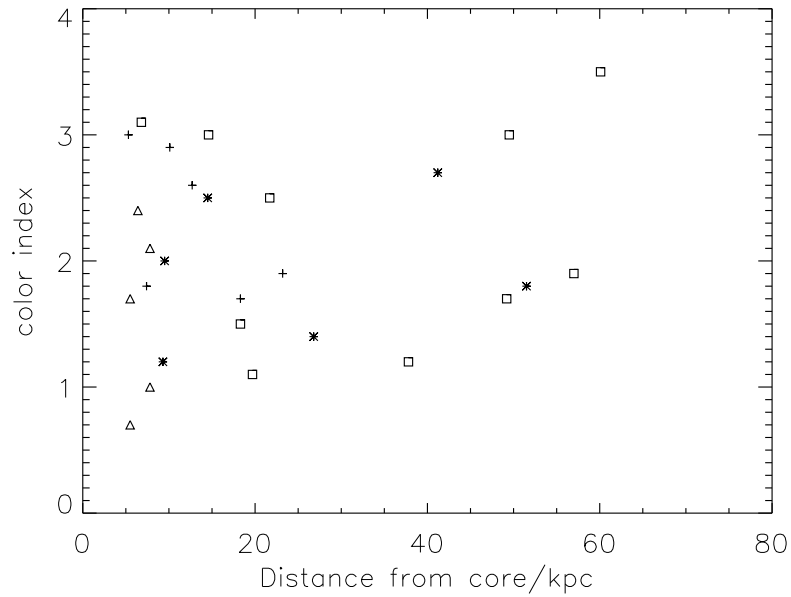


Fig. 31.— The optical-to-infrared color indices of the components of the 4 clumpy radio galaxies MRC 0406–244 (triangles), MRC 1138–262 (squares), USS 1707+105 (asterisks) and MRC 2104–242 (plus), plotted versus their distance from the galaxy radio core (or nucleus).

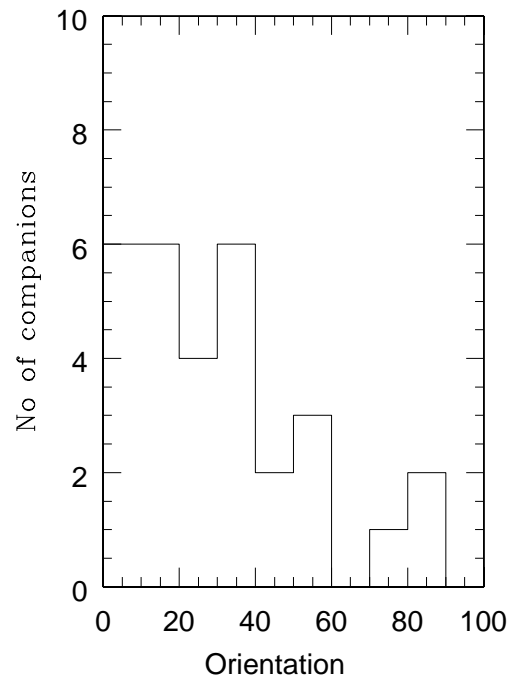


Fig. 32.— Distribution of the orientation of companion galaxies within 50 kpc of the radio galaxies, with respect to the radio axis